Author Contributions:

Formal analysis: E. M. Babu
Writing – original draft: E. M. Babu
Writing – review & editing: E. M. Babu, J. A. Salice, B. Funke

Energetic Electron Precipitation During Slot Region Filling Events

H. Nesse[1] , E. M. Babu[1] , J. A. Salice[1] , and B. Funke[2]

[1]Department of Physics and Technology, University of Bergen, Bergen, Norway, [2]Instituto de Astrofísica de Andalucía, CSIC, Granada, Spain

Abstract The slot region marks the equatorward boundary of the energetic electron precipitation (EEP). There are, however, numerous reports where energetic electrons cross these boundaries and fill the slot region. The ensuing EEP will occur long after the geomagnetic activity subsides. This is a missing energy input in current EEP estimates scaled by geomagnetic indices. This study explores the occurrence rate, duration, and local time dependence of slot region filling events using observations from the National Oceanic and Atmospheric Administration/Polar Orbiting Environmental Satellites over a full solar cycle from 2004 to 2014. The EEP flux estimates are based on the Medium Energy Proton Electron Detector 0° and 90° detectors and the theory of pitch angle diffusion by wave-particle interaction. The occurrence rates of >43, >114, and >292 keV events are found to be strongly energy and solar cycle dependent. Higher energy events are more likely to be associated with Coronal Mass Ejections and stronger geomagnetic deflections compared to lower energy events. Solar wind speed, Bz, and Ey reveal a calm period before the events, potentially important for preconditioning the ensuing magnetospheric mass convection. The slot region reforms more efficiently closer to the plasmapause, which creates a double EEP band throughout the recovery period. The slot region EEP maximizes around noon throughout the afternoon/evening sector, consistent with pitch angle scattering from plasmaspheric hiss and lightning induced whistler mode waves. Concurrent with slot region filling events, the Michelson Interferometer for Passive Atmospheric Sounding/Envisat nitric oxide density show an increase at <55° corrected geomagnetic latitudes. This demonstrates the importance of including slot region EEP when assessing the EEP impact on the atmosphere.

1. Introduction

Energetic electrons in the inner magnetosphere are distributed into two regions: the inner and the outer radiation belt. The outer radiation belt is strongly influenced by the varying solar wind and varies in both content and extent. In contrast, the inner radiation belt is relatively stable. The region separating the inner and outer radiation belt, typically devoid of energetic electrons, is termed the slot region. It results from a balance between inward radial transport due to ultra low frequency waves and atmospheric loss due to plasmaspheric hiss and lightning generated whistlers (Kim et al., 2011). The location of the slot region is energy dependent, but is typically found in an approximate range around $L = 2$–3 (Lyons & Thorne, 1973).

The equatorward boundary of the energetic electron precipitation (EEP) from the outer radiation belt is closely linked to the location of the plasmapause (Babu et al., 2022a; van de Kamp et al., 2016). As the electromagnetic waves strongly depend on the medium they propagate in, the plasmapause marks an abrupt change in the characteristics of the wave-particle interaction (Li et al., 2016; Walton et al., 2021). Chorus and electromagnetic ion-cyclotron (EMIC) waves, which largely govern the EEP processes, tend to occur outside and near the outer edge of the plasmasphere, respectively (Carson et al., 2013; Lam et al., 2010; Whittaker, Rodger, et al., 2014; Whittaker, Clilverd, & Rodger, 2014). They are efficiently damped within the dense cold plasmasphere. Statistical mapping of the EEP region confirms the chorus driven wave pattern (Lam et al., 2010; Li et al., 2016). The plasmapause and the equatorward edge of the EEP is typically parameterized by geomagnetic indices (Babu et al., 2022a; Moldwin et al., 2002; van de Kamp et al., 2016, 2018) or more advanced machine learning algorithms (Chen et al., 2023). There are, however, numerous reports where the energetic electrons cross these boundaries and fill the slot region with energetic electrons. Inside the plasmasphere, plasmaspheric hiss and lightning generated whistlers can scatter the electrons into the atmosphere long after the geomagnetic activity subsides (Babu et al., 2022a; Baker et al., 2004; Kavanagh et al., 2018; Reeves et al., 2016; Turner et al., 2017). These are features precluded in statistical mappings and simple models driven by geomagnetic indices.

During geomagnetic storms, in particular where the outer belt is severely distorted, the slot region can be filled with energetic electrons through a combination of local wave-particle acceleration and inward radial transport (Baker et al., 2004; Thorne et al., 2007). The occurrence rate of a slot region filling events is energy dependent, where lower energy electrons are more likely to penetrate the plasmapause and the slot region compared to higher energies (Reeves et al., 2016; Thorne et al., 2007).

The slot region will gradually reform by plasmaspheric hiss and whistler waves scattering electrons into the atmospheric loss cone (Meredith et al., 2009). The atmospheric loss process after a slot region filling event starts immediately (Reeves et al., 2016). The loss rate is both L-shell and energy dependent. At lower L shells in the slot region, the lifetime of an electron for a given energy is progressively longer (Meredith et al., 2009; Ripoll et al., 2015). In a superposed epoch analysis of 41 Corotating Interaction Region (CIR) driven storms, Ødegaard et al. (2017) revealed potential low latitude precipitation for electron energies of >43 and >114 keV estimated from the Medium Energy Proton Electron Detector (MEPED) onboard the National Oceanic and Atmospheric Administration (NOAA) Polar Orbiting Environmental Satellites (POES). In the High Energy Particle Precipitation in the Atmosphere (HEPPA) intercomparison project, Nesse Tyssøy et al. (2022) compared eight different EEP precipitation estimates ≳30 keV based on MEPED. Large uncertainty in the latitudinal extent of the precipitation region as well as a potential low-latitude precipitation band was disclosed. The period of comparison co-exists with a slot region filling event as identified by Kavanagh et al. (2018). In fact, Kavanagh et al. (2018) and Babu et al. (2022a) show that for >~30 keV electrons slot region filling events and the associated EEP are fairly frequent and long persistent. This represents a missing source of energy in current EEP estimates based on geomagnetic indices.

The ionization caused by EEP initiates a sequence of chemical reactions increasing the production rates of HOx (H, OH, HO_2) and NOx (N, NO, NO_2) radicals in the upper atmosphere (Sætre et al., 2004; Smith-Johnsen et al., 2017; Zawedde et al., 2016). HOx and NOx gasses reduce ozone in catalytic reactions (Sinnhuber et al., 2012; Zawedde et al., 2019). Ozone is important in the local thermal energy budget, which implies that a reduction may alter atmospheric temperature gradients and consequently the breaking of atmospheric waves (Rozanov et al., 2012; Seppälä et al., 2013; Zúñiga López et al., 2022). The latter has the potential of changing the upper stratospheric dynamics through complicated feedback processes, with a possible link to winter surface weather patterns (Maliniemi et al., 2016; Rozanov et al., 2012; Seppälä et al., 2009).

In this study, we quantify the EEP associated with the slot region filling events. In contrast to previous studies estimating the EEP characteristics based on MEPED 0° (Chen et al., 2023; Lam et al., 2010; Li et al., 2016; van de Kamp et al., 2016, 2018), we combine observations from both the MEPED 0° and 90° detectors together with theory of pitch angle diffusion by wave-particle interaction to quantify the EEP flux in the total bounce loss cone (BLC). The MEPED energy channels, >43, >114, and >292 keV, are treated independently to explore the associated energy dependence in terms of occurrence, duration, and latitude extent. The main objective is to identify its characteristics in order to increase the EEP modeling capability. Moreover, we explore to which extent the low latitude slot region EEP is observable in the NO density estimated from the Michelson Interferometer for Passive Atmospheric Sounding (MIPAS) instrument on board the Envisat satellite in order to evaluate its potential impact on the atmosphere.

2. Data and Methods

2.1. Bounce Loss Cone Fluxes Estimated From MEPED

This study applies the second version of the Space Environment Monitor on-board the NOAA/POES and EUMETSAT/MetOp series over a full solar cycle from 2004 to 2014. In this period three to six POES and MetOp spacecrafts circle the Earth at around 800–850 km in a polar sun-synchronous orbit approximately every 100 min. These are POES 15–19 and MetOP-2 covering different parts of the MLT sectors as illustrated in Figure 1. We apply the MEPED instrument which consists of two solid state electron and proton detectors pointing nearly perpendicular to each other, commonly termed as the 0° and 90° detectors (Evans & Greer, 2004).

The field of view of the MEPED telescopes is 30° full width. The nominal energy limits are listed as >30, >100, and >300 keV (Evans & Greer, 2004). The real detector efficiency, however, will depend on the incoming energy spectrum (Yando et al., 2011). Ødegaard et al. (2017) obtain new optimized effective integral energy limits >43, >114, and >292 keV and associated geometric factors based on a series of realistic power law and exponential spectra utilizing Yando et al. (2011)'s modelled detector response. Furthermore, the false counts due to contaminating protons are removed. The observed proton fluxes are first corrected for degradation due to radiation damage by applying correction factors derived by Sandanger et al. (2015) and Ødegaard et al. (2016).
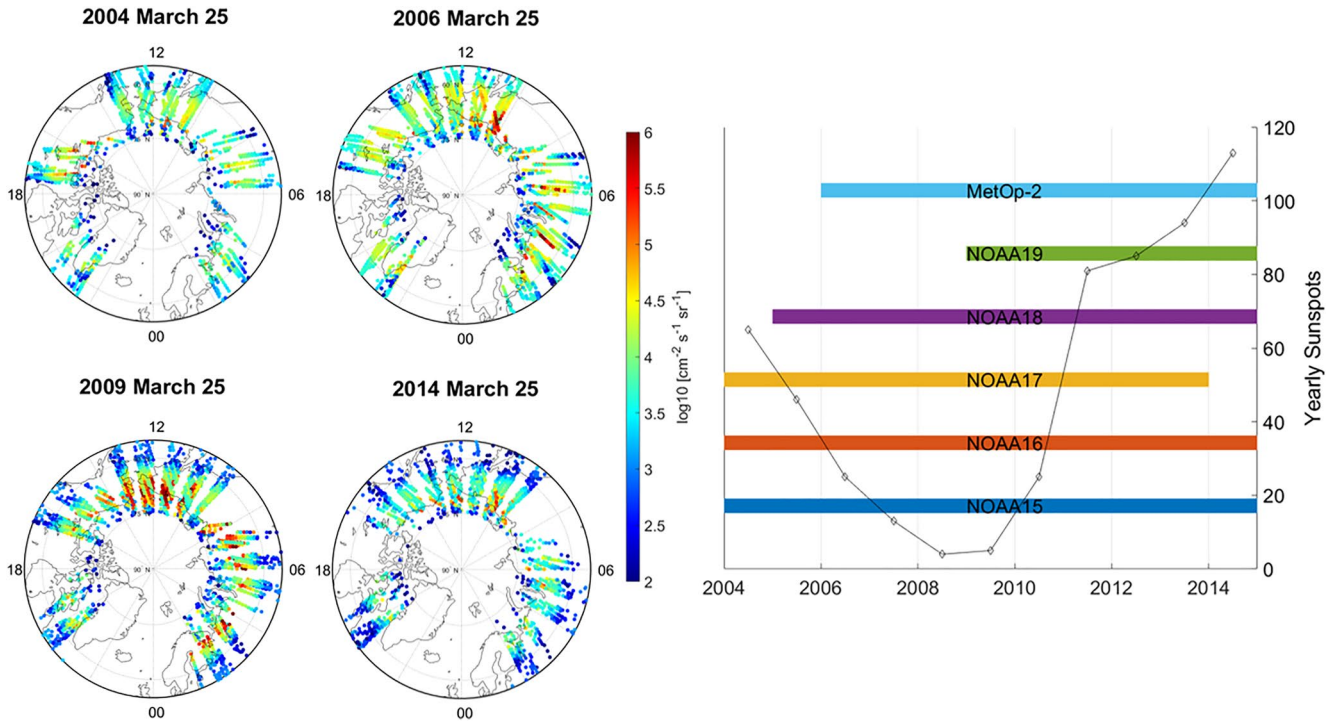
Figure 1. Left: The Polar Orbiting Environmental Satellites (POES) and MetOp satellite MLT coverage over a full day during March 25th in 2004, 2006, 2009, and 2014. Right: The POES and MetOp satellite coverage over a full solar cycle from 2004 to 2014. The figure is a copy of Figure 1 in Babu et al. (2022a).

Subsequently, the proton flux in the energy intervals known to impact the respective electron channels (Evans & Greer, 2004), are then subtracted from the original measured electron fluxes (Nesse Tyssøy et al., 2016).

At middle and high geomagnetic latitudes the 0° telescope detects particles at pitch angles within the BLC, while the 90° telescope detects fluxes at pitch angles both within and outside BLC (Nesse Tyssøy et al., 2016; Rodger et al., 2010). The detectors only observe part of the pitch angle distribution, which makes them both a coarse estimate for the precipitating fluxes. In the common case of an anisotropic pitch angle distribution, the 0° detector will underestimate, while the 90° detector will overestimate the flux of precipitating electrons (Nesse Tyssøy et al., 2016, 2022). A more realistic estimate can be achieved by combining the observed fluxes from both telescopes together with theoretical electron pitch angle distributions calculated based on of wave-particle interactions in the inner magnetosphere. As described in detail in Nesse Tyssøy et al. (2016), the Fokker-Planck equation for particle diffusion (Kennel & Petschek, 1966; Theodoridis & Paolini, 1967) is solved for a wide range of diffusion coefficients. The solutions are then transformed to the satellite altitude and organized in a lookup table. Taking into account the viewing directions of the telescopes relative to the magnetic field and the detector response-function for different viewing angles through the detector collimator, the ratio between the fluxes detected by the 0° and 90° detector is used to identify the theoretical pitch angle distribution that best corresponds to the observations. Finally, the size of the BLC, predicted based on the International Geomagnetic Reference Field model, are applied to estimate the precipitating fluxes. At a specific latitude the size of the BLC changes with longitude due to the variation in the magnetic field strength. Over one drift period, the largest BLC will correspond to the drift loss cone. The BLC flux estimate is done separately for each energy channel as the level of particle diffusion will vary with energy. The daily resolved fluxes are sorted into eight MLT sectors (3-hr resolution) and 1° CGM (corrected geomagnetic) latitude. Note, however, the poor data coverage in the evening (18–21) and pre-midnight (21–24) MLT sector as illustrated in Figure 1.

In this study we will use the BLC flux estimate to indicate when a slot region filling event occurs, its duration, and latitudinal extent. The BLC fluxes will also enable an assessment of the MLT behaviour.

2.2. Identifying the Onset of Slot Region Filling Events

The POES 0° detector has previously been applied to identify slot region filling events. Kavanagh et al. (2018) used flux observations above the detector's noise level at $L = 2.7$ alongside an identifiable increase over a wide

range of low *L*-shells as criteria. The location of the inner edge of the outer radiation belt, however, varies strongly with geomagnetic activity. To separate the regular outer radiation belt distortion from the extraordinary slot region filling events, we wish to account for the expansion and shrinking of the radiation belt when identifying the events.

Babu et al. (2022a) identifies the Northern Hemisphere (NH) equatorward boundary for the EEP precipitation region for the full solar cycle from 2004 to 2014. The boundary is defined as the geomagnetic latitude where the flux rises above a threshold value with a poleward positive gradient. The threshold value corresponds to two standard deviations above the mean flux level at 50°–60° CGM latitude during ambient solar wind conditions. Babu et al. (2022a) frequently observed, local maxima at low latitudes after which the equatorward boundary had been very low. The slowly decaying low-latitude maxima appeared independent of the strongly varying solar wind properties and geomagnetic activity. These occurrences were assumed to be remnants after slot region filling events. In these cases Babu et al. (2022a) chose the second threshold crossing as the equatorward boundary. Moreover, the period preceding the double maxima was labelled ambiguous and not part of the data that formed the basis for the empirical model scaled by pressure corrected Dst. In this study, we include these ambiguous periods utilizing the full database of the identified equatorward boundary from Babu et al. (2022a).

We use energy channel >43 and >114 keV to identify possible events. As the inner edge of the outer radiation belt are normally expected to track the average location of the plasmapause, we compare the observed equatorward boundary to the expected movement of plasmapause using the model by Moldwin et al. (2002). The plasmapause model is scaled by Kp independent of MLT. We use fluxes from the post-midnight sector (0–3 MLT) as the injection takes place on the night side. Here, the plasmapause location modelled by Moldwin et al. (2002) are in line with more advanced dynamical plasmapause models such as for example, Liu et al. (2015). The mean differences between the equatorward latitude boundary of the EEP region as identified by Babu et al. (2022a) and the plasmapause location is found to be 3.7° and 4.3° for >43 and >114 keV electron fluxes, respectively. The associated standard deviations are 3.2° and 3.1°. We identify potential slot region filling events as periods where the equatorward boundary and the estimated plasmapause latitude are separated more than the mean plus one standard deviation for either or both >43 and >114 keV (Single days are automatically disregarded). The onset is chosen as the day where the Dst drop is the largest (This two step process is illustrated in Figure 2). This resulted in an initial pool of 106 potential events. However, 21 events were discarded as they were not associated with a drop in the Dst (ΔDst* > −6 nT) or occurred within 4 days of the previous event. Eighteen events that occurred in the same period as a solar proton event were discarded. Moreover, two events were discarded based on missing data at the start of the event. In total, this resulted in 65 > 43 keV events from 2004 till 2014 listed in Table 1. Fifty-five and 32 of these events were evident also in the >114 and >292 keV fluxes, respectively.

Note, that in contrast to Kavanagh et al. (2018) we do not have an explicit flux threshold requirement. It is, however, implicitly included as the equatorward boundary identification in Babu et al. (2022a) includes a threshold value corresponding to two standard deviation above the mean flux level 50°–60° CGM latitude during ambient solar wind conditions.

2.3. Estimating the Duration of a Slot Region Filling Event

The frequency of the slot region filling events makes it hard to determine their duration. In the declining phase of the solar cycle, a new event often occurs before the previous one has ended. Therefore, to assess the duration, we wish to select isolated events or the events that is last in a sequence. An event is assumed to be isolated or the last of a sequence, if the daily Dst drop is less than −15 nT for 14 days following the event. Moreover, to evaluate potential energy dependency, the same event list is used for each energy channel. This implies that only events that are also evident in the >292 keV are selected. Fourteen events meet these criteria. We assume that the events have ended when the initial maximum flux below 57° CGM latitude is reduced by a factor of four. Selecting the maximum flux injected and precipitated below 57° CGM latitude, instead of the pre-event flux level, removes potential bias related to events occurring as the last of a sequence.

2.4. MIPAS NO Observations

The nitric oxide (NO) observations in this study have been obtained from the MIPAS instrument on board European Space Agency's Envisat satellite. The instrument has been operational during 2002–2012, measuring infrared (IR) emissions from the atmosphere in the wavelength range of 4.15–14.6 µm in limb viewing geometry (Fischer et al., 2008). We use the latest version of MIPAS 5.3 µm data from nominal measurement mode (NOM,
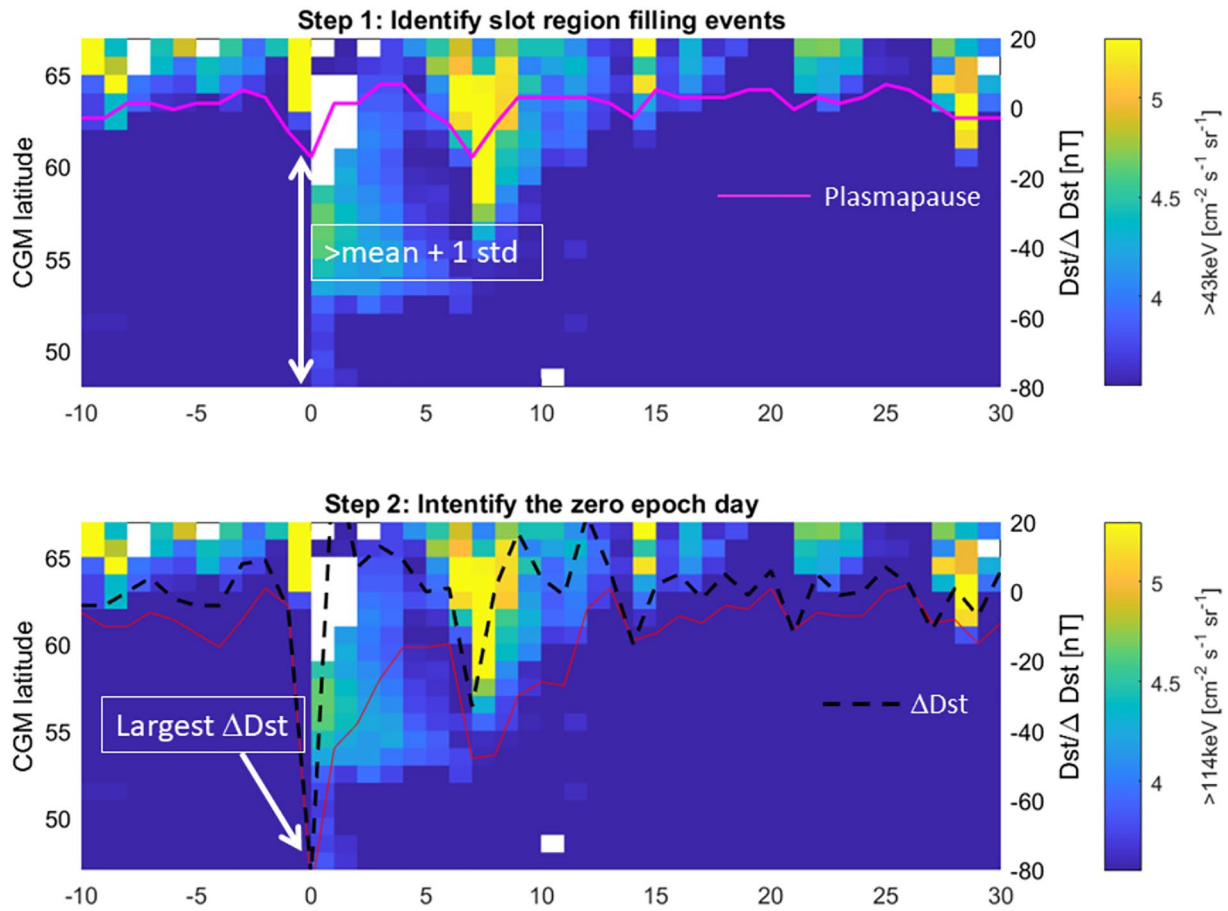
Figure 2. Illustration of process of identifying the slot region filling events. Step 1: We identify potential slot region filling events as periods where the equatorward boundary and the estimated plasmapause latitude are separated more than the mean plus one standard deviation for either or both >43 and >114 keV. Step 2: The onset is chosen as the day where the Dst drop is the largest. The illustrated event has zero epoch day 25 October 2011.

data version V8R_NO_261). This data set covers NO volume mixing ratio (VMR) measurements in the 5–70 km altitude range from 2005 to early 2012 (see Funke et al. (2022) for a complete description).

For this study, we average NO VMR measurements in the altitude range 60–70 km and bin them into CGM latitude bins with daily resolution. The VMR of NO in the mid- and the high-latitude middle atmosphere is dependent on the season due to NO destruction from photolysis and its associated daylight chemistry during sun-lit periods (Brasseur & Solomon, 2005; Smith-Johnsen et al., 2017). Therefore, the yearly NO VMR data will have a strong seasonal dependency. The climatology is based on the mean NO VMR during 2005–2011 applying a 14-day moving average (illustrated in Figure 3) to dampen individual events. To investigate the NO response to slot region filling events, VMR changes with respect to the seasonal climatology (Figure 3) are considered. We achieve this by calculating the percentage increase in NO VMR from the following equation:

$$[NO]_{\%increase} = \frac{[NO] - \overline{[NO]}_{14Day}}{\overline{[NO]}_{14Day}} \times 100, \qquad (1)$$

where [NO] is the NO VMR for each year during 2005–2011 and $\overline{[NO]}_{14Day}$ is calculated by taking a 14-day moving average of NO VMR for individual years and then averaging them.

3. Results

Figure 4 shows the superposed epoch analysis of 65, 55, and 32 identified slot region filling events for >43, >114, and >292 keV BLC fluxes, respectively. The onset day is characterized by deep continuous precipitation over a

Table 1

List of Identified Slot Region Filling Events From 2004 to 2014 Based on Bounce Loss Cone Electron Estimates of >43, >114, and >292 keV

Slot region filling events from 2004 to 2014					
>43 keV	>112 keV	>292 keV	>43 keV	>112 keV	>292 keV
1/22/04	Yes	–	4/5/10	Yes	Yes
2/11/04	Yes	Yes	4/12/10	Yes	Yes
3/10/04	Yes	Yes	5/4/10	Yes	Yes
3/28/04		–	5/29/10	Yes	–
4/3/04	Yes	Yes	8/4/10	Yes	Yes
7/17/04	Yes	–	4/12/11	Yes	–
7/23/04	Yes	Yes	4/30/11	Yes	–
8/30/04	Yes	Yes	5/28/11	Yes	Yes
9/22/04		–	9/10/11	Yes	–
1/8/05	Yes	–	9/17/11	Yes	Yes
2/7/05	Yes	–	10/25/11	Yes	Yes
3/6/05	Yes	Yes	11/1/11	–	–
4/5/05	Yes	Yes	2/16/12	Yes	–
4/12/05	Yes	–	3/28/12	Yes	–
5/8/05	Yes	Yes	4/5/12	Yes	–
5/30/05	Yes	Yes	4/13/12	–	–
6/13/05	Yes	Yes	4/24/12	Yes	Yes
7/9/05	Yes	Yes	6/11/12	Yes	–
8/10/05	Yes	–	6/30/12	–	–
8/31/05	Yes	–	10/8/12	Yes	Yes
4/5/06	Yes	Yes	10/13/12	Yes	Yes
4/14/06	Yes	Yes	11/14/12	Yes	Yes
4/22/06	Yes	Yes	3/29/13	Yes	Yes
6/6/06	Yes	–	5/1/13	Yes	Yes
7/28/06		–	6/1/13	Yes	Yes
8/20/06	Yes	Yes	6/7/13	Yes	Yes
11/30/06	Yes	Yes	7/6/13	Yes	Yes
3/24/07	Yes	–	7/10/13	Yes	–
7/15/07	Yes	–	8/28/13	–	–
3/1/08	Yes	–	11/9/13	–	–
3/9/08	Yes	–	2/19/14	Yes	–
3/27/08	Yes	–	5/8/14	–	–
7/22/09		–	–	–	–

Note. Events with concurrent Solar Proton Events were excluded.

wide range of latitudes extending below 50°N CGM latitude for all energies. The precipitating electrons >292 keV, however, achieve maximum intensity the succeeding day. In the following days the precipitation band becomes narrower. Moreover, a two-band structure emerges as the precipitation from the slot region displays a local maximum. The local maximum is found at lower latitudes for higher energies. The slot region re-forms faster close to the main precipitation region which is known to closely follow the plasmapause movement. Consistent with previous reports by for example, Reeves et al. (2016), Turner et al. (2017), Babu et al. (2022a) the occurrence rate of slot region filling events is expected to be higher for lower energies. Based on our slot region event identification criteria, >43 keV events has twice the occurrence rate than >292 keV events. The average Dst index (plotted as a red solid line on top of the color plot) shows that the Dst minima are less prominent for >43 keV events, compared to > 292 keV events. On the zero epoch day, the daily Dst is on average −43, −45 nT, and −52 nT for >43, >114, and >292 keV events, suggesting that stronger geomagnetic storms are required to drive slot region filling events for relativistic electrons.

Our identification of slot region filling events is based on the precipitating fluxes in the post-midnight sector as the injection takes place on the night side. Figure 5 displays how the identified events evolve in time at all MLTs. The thin bright yellow line marks the estimated plasmapause location scaled by Kp as modelled by Moldwin et al. (2002). At zero epoch day, the intensification of low latitude precipitation is evident at all MLTs. However, in the following days an MLT dependent precipitation pattern emerges at latitudes linked to both the radiation belt and the plasmasphere. The MLT dependence is more prominent in the >43 keV compared to >292 keV EEP. In the main EEP band, poleward of the plasmapause, the >43 keV electron precipitation maximizes in the morning sector and minimizes in the afternoon sector, where >292 keV electron precipitation appears more homogeneous. In contrast, for both >43 and >292 keV weaker precipitation is found in the morning MLT sectors 3–6 and 6–9 at latitudes equatorward of the estimated plasmapause, while stronger precipitation occurs in the noon and afternoon/evening sectors. This is highlighted in Figure 6 which shows the same data as Figure 5 for epoch days 6, 8, and 10 with a different color scale to emphasize the EEP MLT pattern at low CGM latitudes. It clearly demonstrates that different pitch angle scattering processes are responsible for the precipitating electrons outside and inside the plasmasphere. Moreover, it is evident that the slot region reforms more efficiently closer to the plasmapause boundary as the precipitation display a local minimum here. This causes two bands of precipitation. The majority of precipitating electrons are linked to the outer radiation belt, whereas a weak drizzle of fairly steady flux levels origins from within the plasmasphere, until the slot region slowly reforms.

It is not straightforward to estimate how long it takes for the injected electrons to be lost to the atmosphere and depleted from the slot region. Often a new event replenish the slot region before it is fully reformed. Hence, we target isolated events or events that are last in a sequence by ensuring that daily Dst change is larger than −15 nT for 14 days after the event onsets. Moreover, as wave-particle interactions are dependent on the electron energies, so might the reformation time. Hence, to compare the energy dependence of the electron lifetime, events that occur in all three energy channels, >43, 114, and >292 keV are selected. Only 14 events fill these requirements as shown in the superepoch analysis in Figure 7. We assume that the event ends when the initial maximum flux below 57° CGM latitude is reduced by a factor of four. This criteria gives a reformation time of 13, 14, and 17 days for the >43, 114, and >292 keV, respectively. Modifying the criteria in respect to daily Dst change or the period it is evaluated, changes the number of events, but there is a consistency
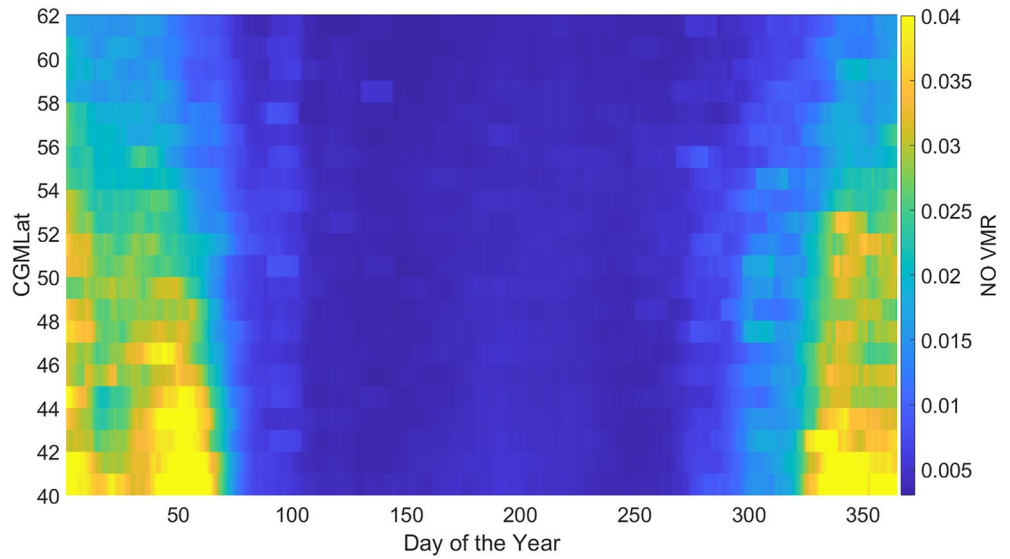
Figure 3. Seasonal climatology plot of 14-day moving mean nitric oxide volume mixing ratio (in ppmv) during 2005–2011 in the northern hemisphere.
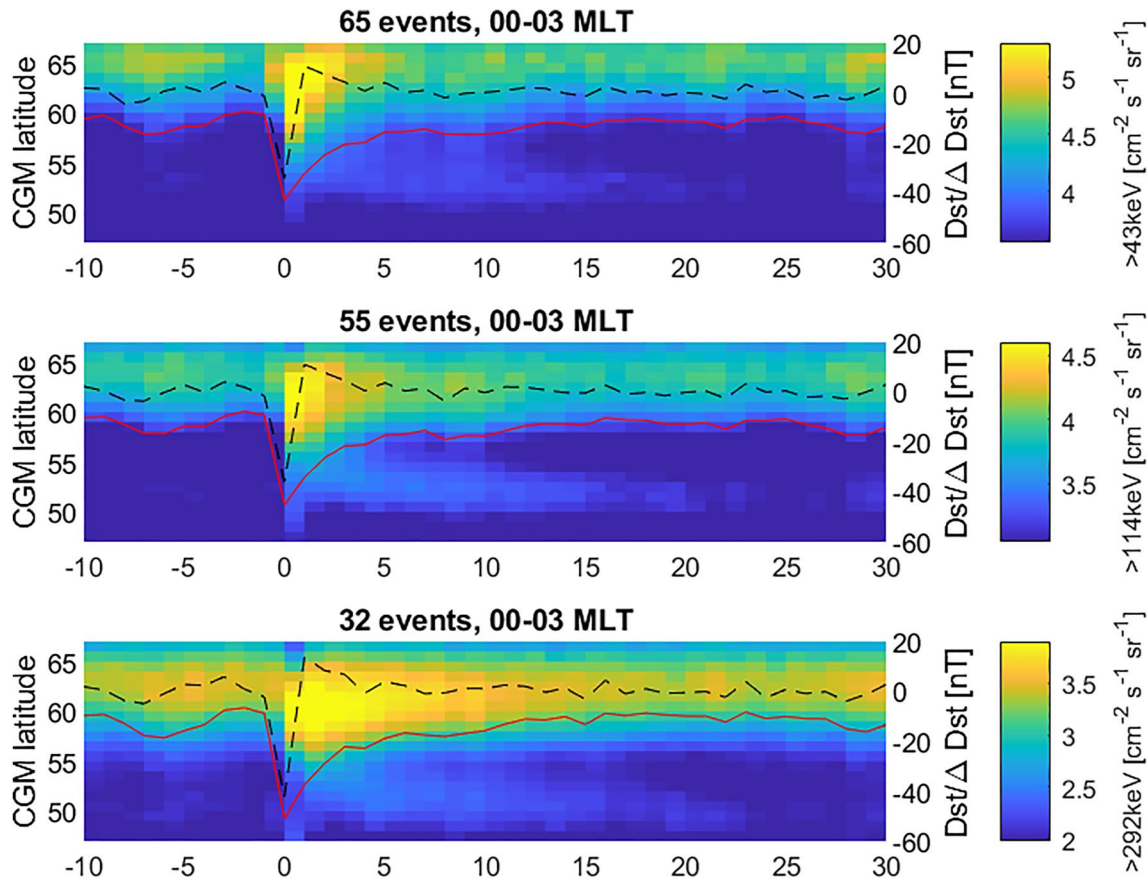

Figure 4. Superposed epoch analysis of identified slot region filling events for >43, >114, and >292 keV fluxes based on the bounce loss cone fluxes for northern hemisphere in the period 2004–2014 displayed from top to bottom panels, respectively. Note that the flux values are given as logarithmic scale. The associated Dst and the time derivative of the Dst are displayed as a solid red and dashed black line, respectively. All data is shown with 1 day resolution.
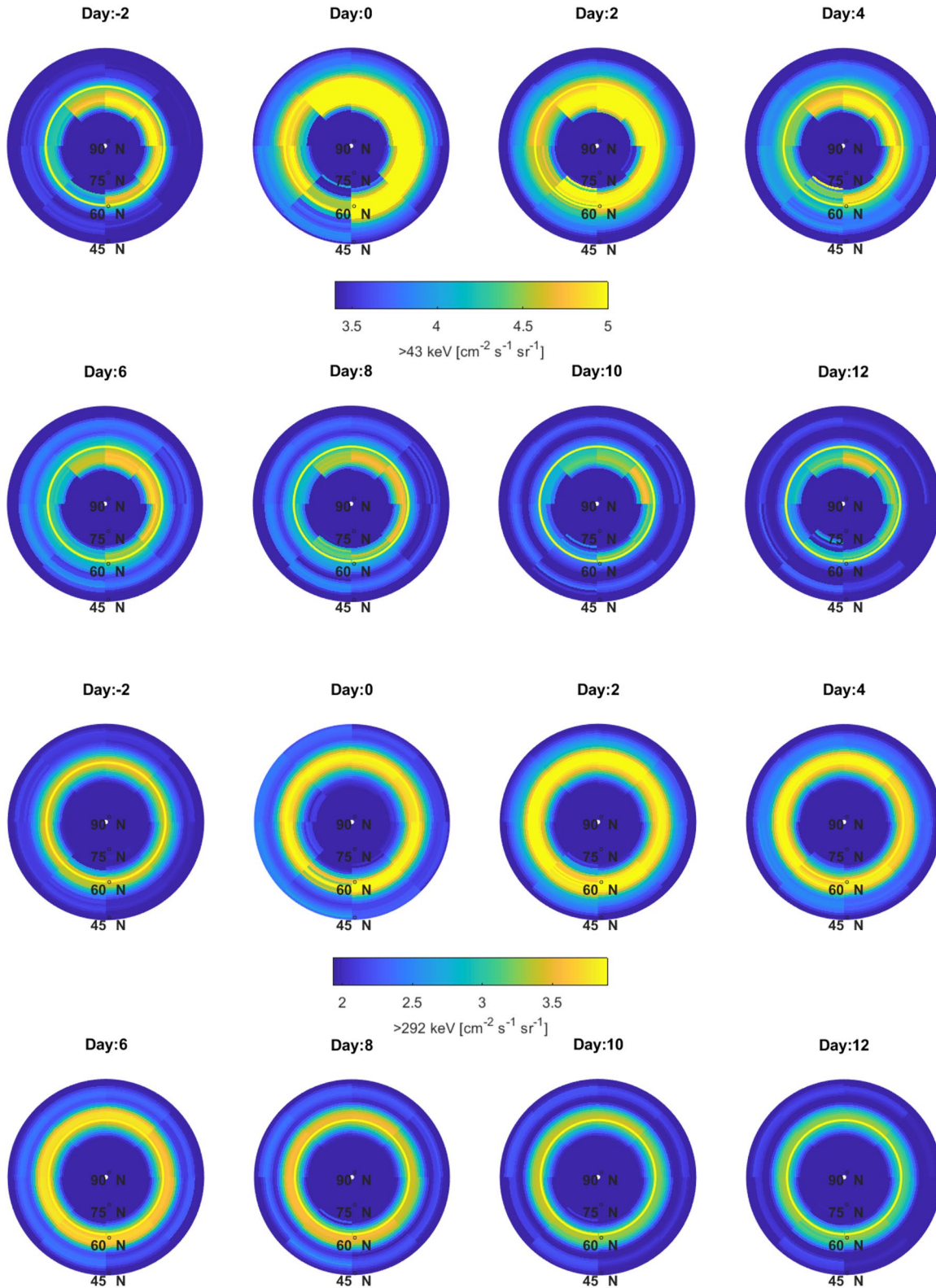
Figure 5. Superposed epoch analysis of identified slot region filling events for >43 keV (eight upper panels) and >292 keV (eight lower panels) based on the bounce loss cone fluxes for northern hemisphere in the period 2004 to 2014. Note that the flux values are given as logarithmic scale.
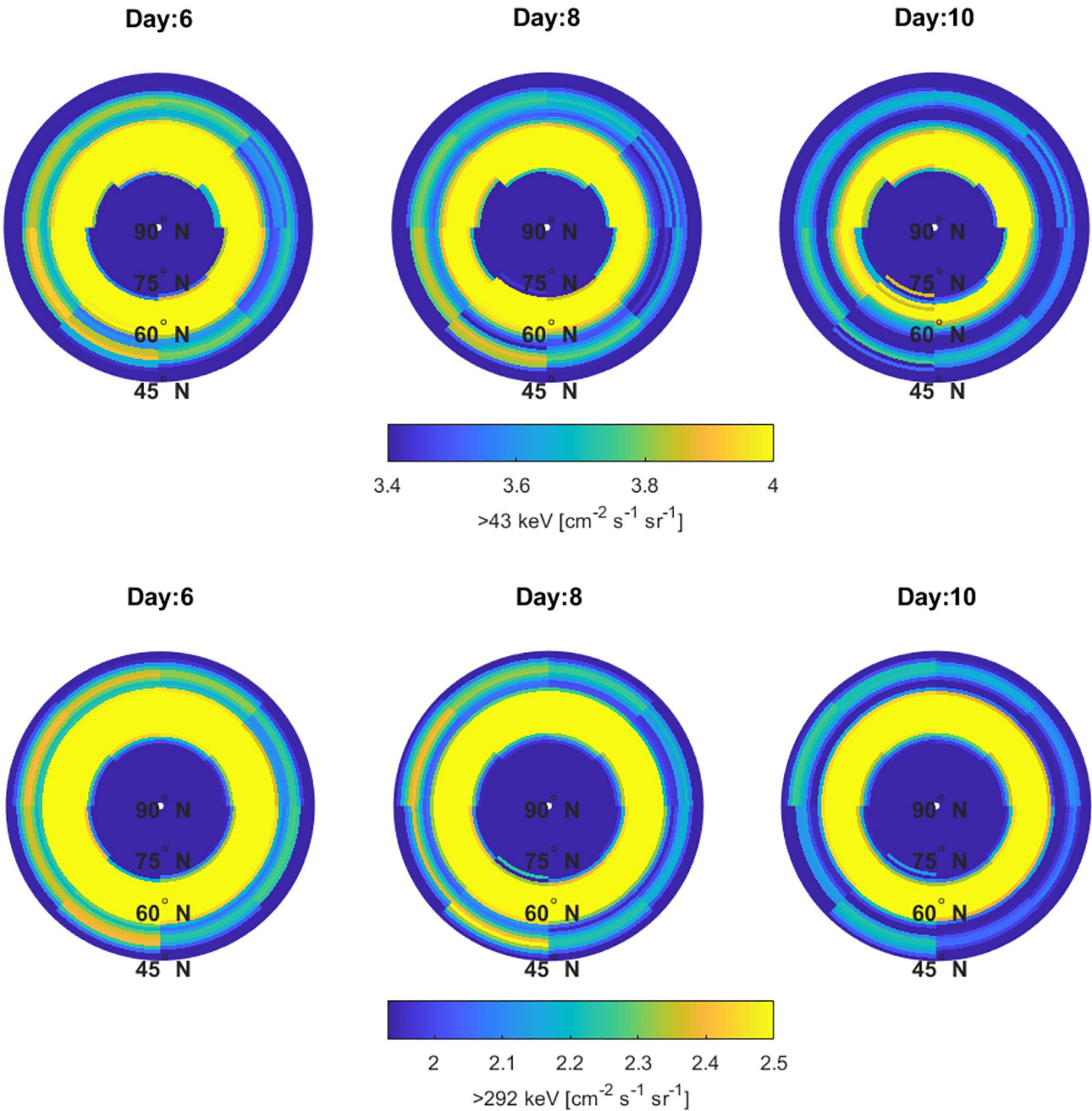
Figure 6. Same as Figure 5 for epoch days 6, 8, and 10 with a different color scale to emphasize the energetic electron precipitation at low corrected geomagnetic latitudes. Note that the flux values are given as logarithmic scale.

of a slightly longer reformation period associated with higher energies. The same assessment holds for changing the relative reduction factor in respect to the zero epoch maximum.

3.1. Dependency on Solar Wind and Geomagnetic Activity

The yearly occurrence rate of the slot region filling events possess a strong solar cycle dependence as illustrated in Figure 8. For the years 2004–2014 the maximum number of events is found in 2005 for all energies. A strong drop in the occurrence rate is evident in the solar minimum years of 2007–2009. In this period, no slot region filling events are found at for the >292 keV fluxes. This is also the case for the unusual weak year of 2014.
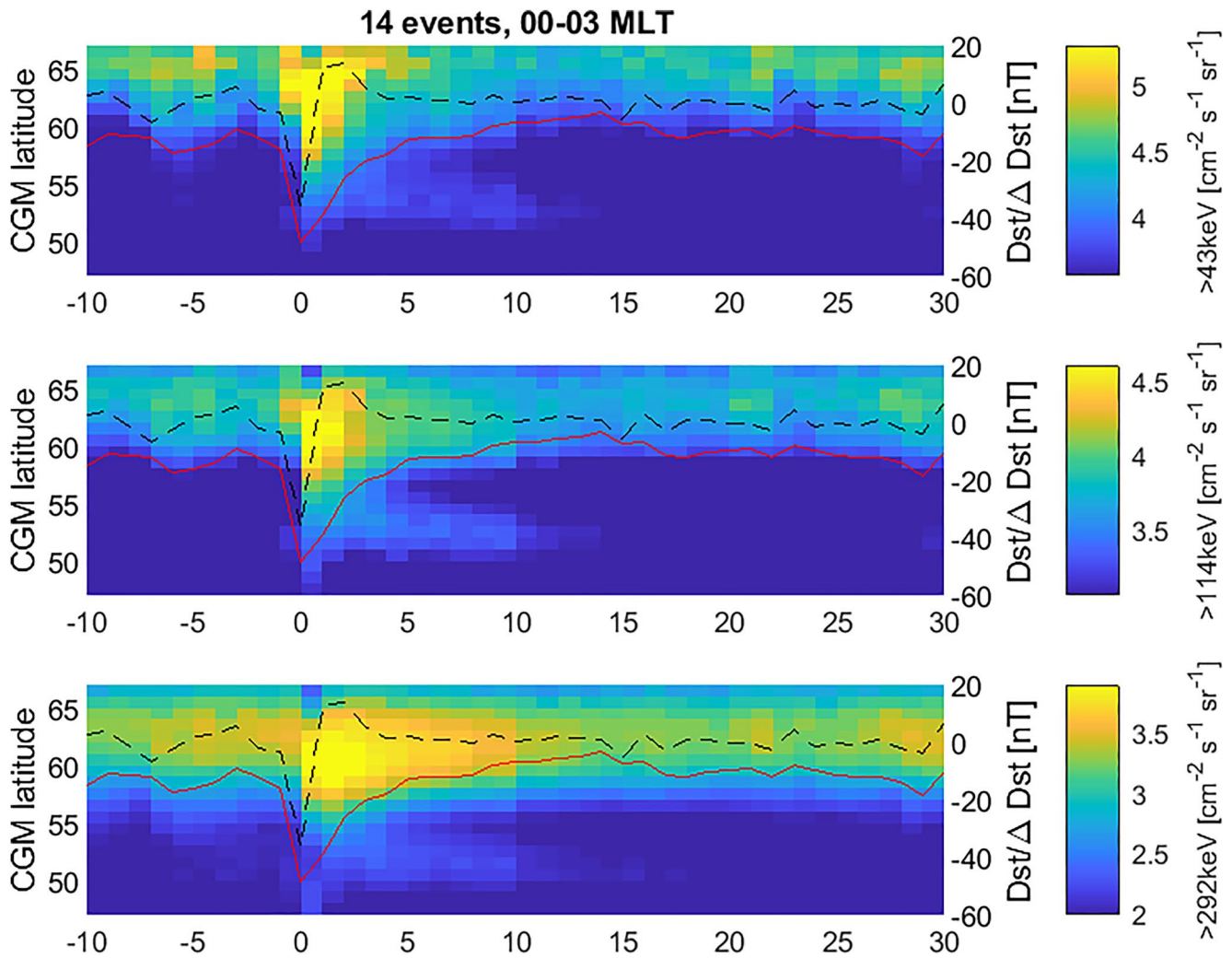
Figure 7. Superposed epoch analysis of 14 slot region filling events concurrent for >43, >114, and >292 keV fluxes displayed from top to bottom panels, respectively. Note that the flux values are given as logarithmic scale. The 14 events are either isolated or the last in a sequence of events, where the daily Dst change is larger than −15 nT. The associated Dst and the time derivative of the Dst is displayed as a solid red and dashed black line, respectively. All data is shown with 1 day resolution.

Moreover, Figure 9 examines the occurrence rate dependency on solar wind drivers. Richardson and Cane (2012) separates solar wind structures into three categories: Coronal Mass Ejections (CMEs), High Speed Solar (HSS) wind or Corotating Interaction Regions (CIRs), and slow ambient solar wind. The identification is based on solar wind parameters, geomagnetic indices retrieved from the NASA OMNIweb database, and observations of cosmic rays with energies between ~0.1 and 1 GeV. In case, the solar wind driver is influenced by both a CME and HSS/CIR, it will label it as a CME. All of the identified slot region filling events are coincidental with a period of either CME or HSS/CIR. For the >43 keV events 33 of 65 events occur in a period dominated by CMEs. For >114 keV 30 of 55 events are driven by CMEs. For >292 keV as many as 21 of 32, corresponding to 65% of the events, are driven by CMEs.

The superposed epoch analysis of the corresponding Dst, Kp, AE, solar wind speed, Interplanetary Magnetic Field (IMF) Bz, and IMF Ey is shown in Figure 10 for >43, >114, and >292 keV slot region filling events. Ey can be considered as a simple energy coupling parameter dependent on solar wind speed and IMF Bz. All parameters display a systematically stronger deflection on the zero epoch day associated with higher energy slot region filling events. The geomagnetic indices intensifies between ~10%–20% for the >292 keV events compared to the >43 keV events. The IMF Ey increases by more than 30% which can mainly be ascribed to a more negative Bz component associated with the higher energy events. This is consistent with a larger fraction of the >292 keV events being driven by CMEs. The solar wind speed has a strong positive gradient reaching a maximum the following day. Moreover, the days preceding the zero epoch appears to be characterized by slow solar wind with consist-
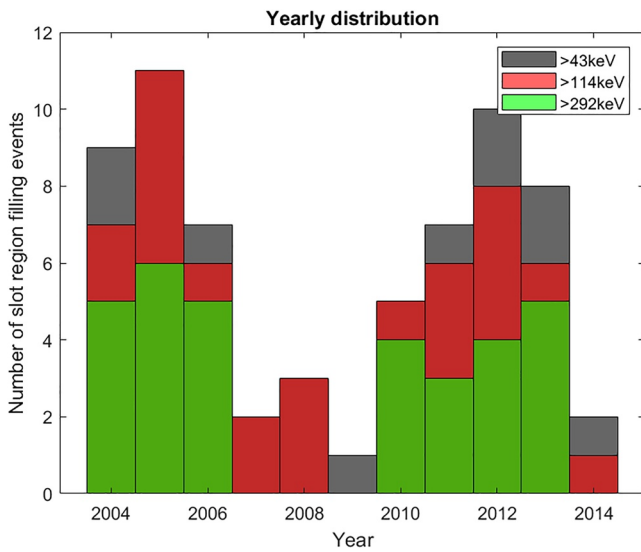
Figure 8. Yearly distribution of the slot region filling events for >43 keV (black bars), >114 keV (red bars), and >292 keV (green bars) for bounce loss cone electron fluxes for the period 2004–2014.
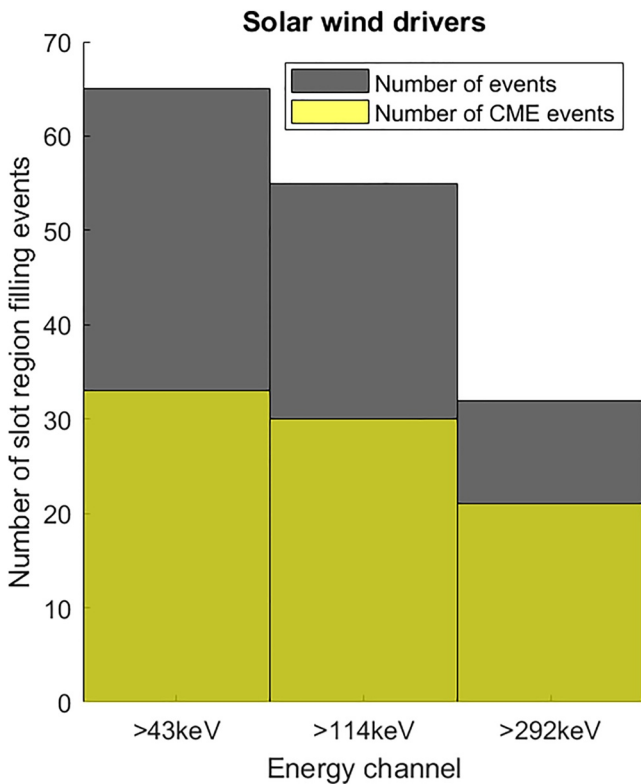

Figure 9. Number of slot region filling events for the period 2004–2014 for >43, >114, and >114 keV (black bars) bounce loss cone electron fluxes. Number of coincidental Coronal Mass Ejection periods (yellow bars) as identified by Richardson and Cane (2012).

ently weak solar wind speed for all events constituting the epoch analysis. This calm before the events alongside a gradual increase of the solar wind are more typical characteristics of CIR events compared to CMEs which often represent more shock like characteristics (Kataoka & Miyoshi, 2006). Shock-like features will, however, be averaged out on the daily scale applied in this study.

Similarly to Figures 10, Figure 11 shows the superposed epoch analysis geomagnetic indices, Dst, Kp, and AE, as well as the selected solar wind parameters, solar wind speed, v, IMF Bz, and Ey, but now divided according to the respective solar wind drivers. The maximum solar wind speed is on average ~90, 100, 110 km/s higher in CIR/HSS events compared to CMEs for >43, >114 and >292 keV. Oppositely, the Bz has a stronger southward component in CME-driven compared to CIR-driven slot region events, which in total results in a stronger Ey value on the zero epoch day. Interestingly, the differences in the geomagnetic indices are less pronounced. In particular, Kp is on average nearly identical for the two solar wind drivers for all the slot region events independent of energy.

3.2. Atmospheric Effects of Slot Region Energetic Electron Precipitation

The sustained EEP supporting the reformation of the slot region has the potential of adding to reactive species like NOx and HOx that can reduce the ozone density throughout the mesosphere and upper stratosphere. It is, however, not straightforward to reveal a potential NO signature for the slot region EEP. The MIPAS 5.3 μm NO VMR estimates from 2005 to early 2012, overlap with 36 of the 65 identified >43 keV slot region filling events. The events occur during all four seasons, with a strong variability of the background NO level. Hence, we use all the data from 2005 until 2011 to create a climatology which enables us to examine the relative change of NO VMR.

The upper boundary of the nominal MIPAS 5.3μm NO observations is approximately 70 km. The maximum ionization rate corresponding to 300 keV electrons is around 70 km (Xu et al., 2020), which implies that the >292 keV electron fluxes best correspond to the upper range of the MIPAS NO observations. Figure 12 includes two plots where the upper panels show the superposed epoch analysis of the >292 keV BLC fluxes as a function of time and latitude. The purple line gives the percentage change relative to the estimated climatology at 40–57° CGM latitude in the altitude range 60–70 km. The lower panel shows the latitude distribution of the NO change. In order to evaluate a potential source of additional ionization by solar flares at mid and low latitudes, the purple line gives the corresponding solar flare index. The upper and lower plots divide the 36 events into 50 percentile high and low >292 keV fluxes below 55° CGM latitude on the zero epoch day (Note that the chosen color scale renders the 50 percentile low >292 keV fluxes dark blue 55°, but the events are still associated with weak low latitude precipitation). For the high >292 keV fluxes, the NO density percentage change increases at all latitudes. In the interval below 57° the increase is >40% relative to the climatology on the zero epoch day and stays elevated >30% throughout the first 4 days of the slot region filling events. A potential second intensification is found around days six and seven prolonging the elevated flux level to around day 11. Similar increase is found on the zero epoch day also for the lower flux levels. However, the NO changes are small from day four and onward. In both cases the solar flare index peak after the initial zero epoch NO increase which makes the EEP the likely source of the
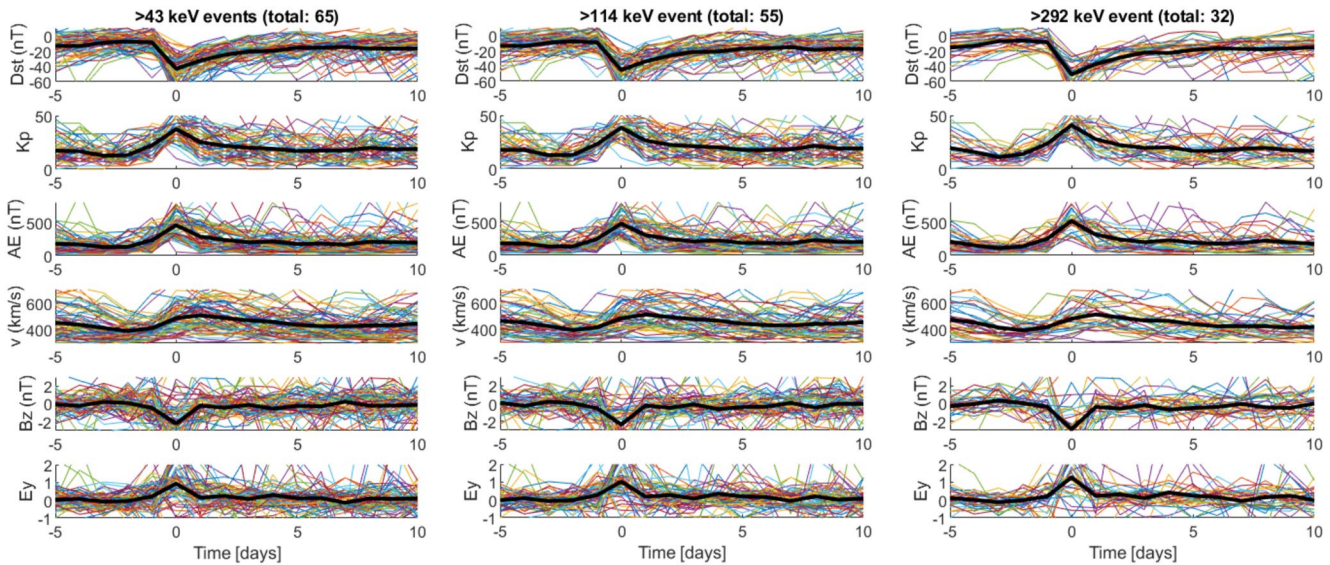
Figure 10. Superposed epoch analysis (black solid line) of the geomagnetic indices, Dst, Kp, and AE, as well as the selected solar wind parameters, solar wind speed, v, Interplanetary Magnetic Field Bz, and their product Ey. The right to left panels show the superposed epoch analysis for the >43, 114, and >292 keV events, respectively alongside the values for the individual events (thin coloured lines).

observed NO increase at all latitudes. It is, however, difficult to assess how long the elevated NO density persists. In the case of high >292 keV fluxes, the NO density is slightly elevated before the zero epoch. This might be partly due to cases where a series of slot region filling events occur within a relatively short time frame.

Moreover, the events included in Figure 12 have a varying degree of exposure to photolysis which will impact the level of NO increase and the associated lifetime. Figure 13 shows that only 10 events occur in NH winter (October–March) and 26 occur in NH summer (April–September). It is readily evident that the winter events on average have weaker >292 keV fluxes compared to the summer events. Nevertheless, both groups show elevated NO levels >40% below 57° CGM latitude. The timing of the maximum is, however, delayed by 1 day during winter, possibly due to prolonged lifetimes and subsequent accumulation of NO molecules over time. The
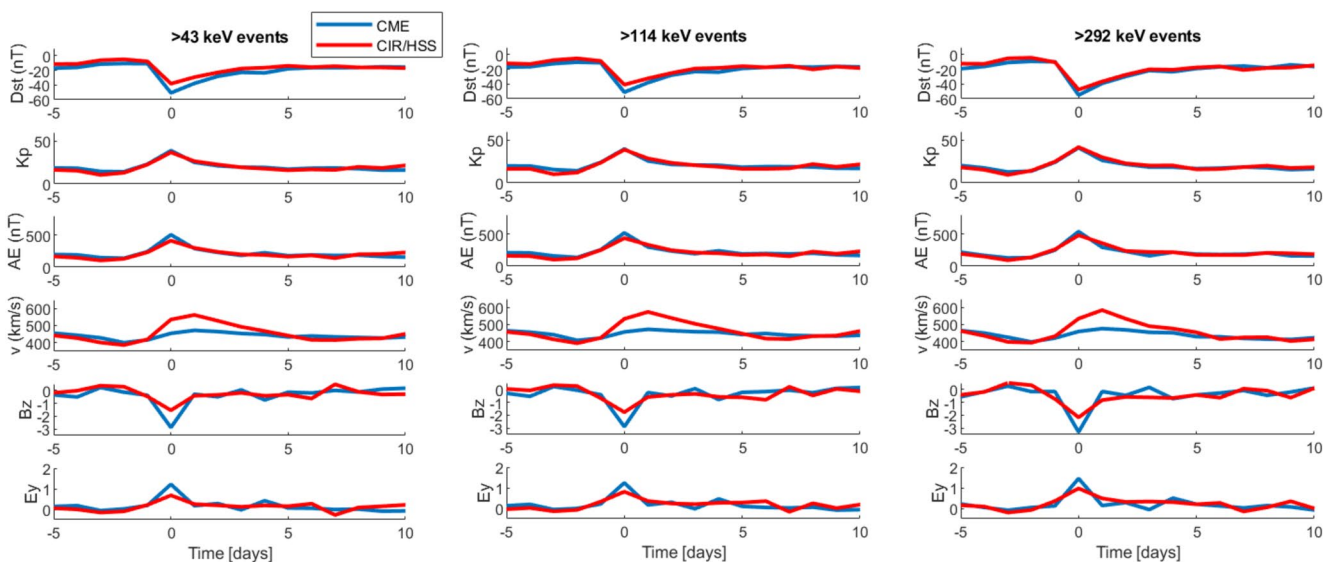

Figure 11. Superposed epoch analysis of the geomagnetic indices, Dst, Kp, and AE, as well as the selected solar wind parameters, solar wind speed, v, Interplanetary Magnetic Field Bz, and their product Ey associated with Coronal Mass Ejection (blue lines) and Corotating Interaction Region/High Speed Solar (red lines) drivers. The right to left panels show the superposed epoch analysis for the >43, 114, and >292 keV events, respectively.
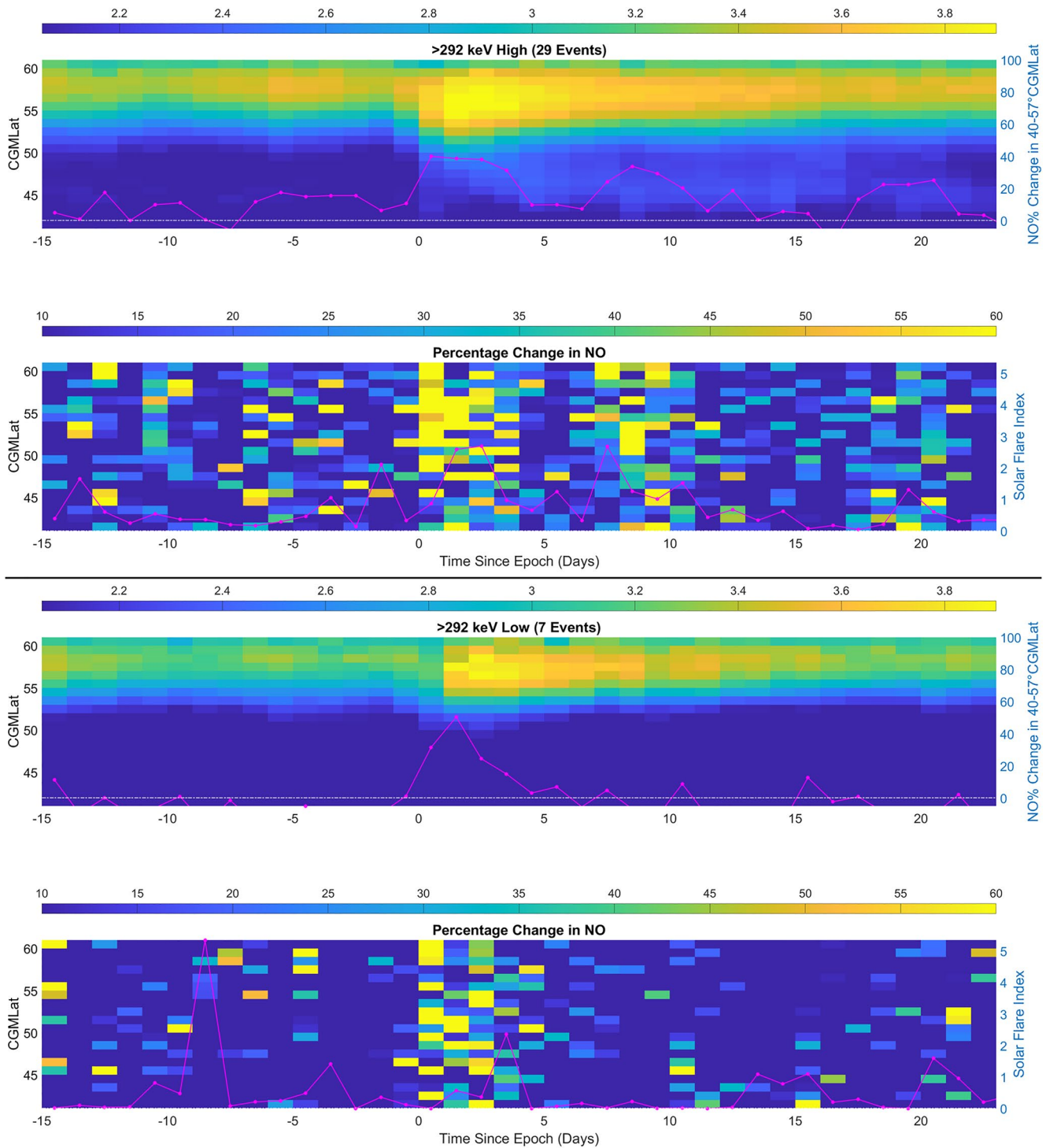
Figure 12. Two plots showing the superposed epoch analysis >292 keV bounce loss cone fluxes and the nitric oxide (NO) percentage change for 50 percentile low and high fluxes. The upper panel in each plots illustrates the flux intensity as function of epoch day and corrected geomagnetic (CGM) latitude. The percentage change in NO density in the region 40–57° CGM latitude relative to the climatology is plotted as a solid purple line. The lower plot shows the time-latitude distribution of the percentage NO change. The solar flare index is given as a solid purple line.

elevated NO density displays a long duration during winter, but it is difficult to link it solely to the slot region EEP of >292 keV fluxes. The solar flare index increases in the same period. Moreover, the longlived NO molecules can be transported from above by the residual winter circulation.
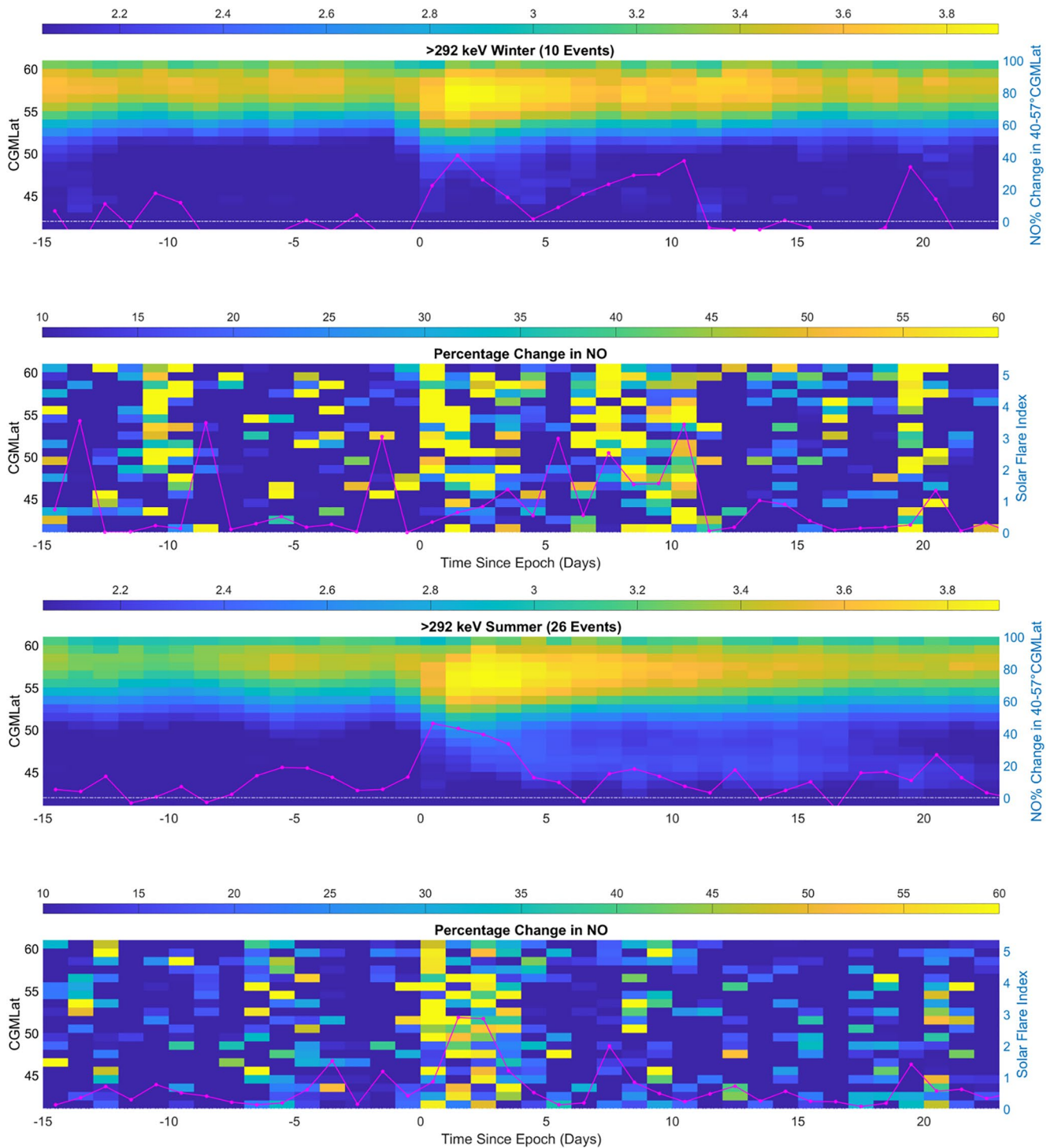
Figure 13. Two plots showing the superposed epoch analysis >292 keV bounce loss cone fluxes and the nitric oxide (NO) percentage change for winter and summer events. The upper panel in each plots illustrates the flux intensity as function of epoch day and corrected geomagnetic (CGM) latitude. The percentage change in NO density in the region 40–57° CGM latitude relative to the climatology is plotted as a solid purple line. The lower plot shows the time-latitude distribution of the percentage NO change. The solar flare index is given as a solid purple line.

4. Discussion

4.1. Solar Wind Drivers and Geomagnetic Activity

Sudden electron flux enhancements at low L shells have been shown to be a common feature of the inner magnetosphere dynamics (Babu et al., 2022a; Kavanagh et al., 2018; Reeves et al., 2016; Turner et al., 2015, 2017). Similarly to for example, Reeves et al. (2016) and Kavanagh et al. (2018) we find that flux enhancements in the slot region are fairly frequent for tens of keV electrons. Figure 3 in Reeves et al. (2016) shows that at least 12 events cause flux enhancement at $L = 2.5$ for 46 keV electrons throughout 2013. We identify 12 potential slot region filling events at >43 keV in the same year where four were discarded based on potential contamination of SPEs. Reeves et al. (2016) shows that the occurrence rate drops monotonously for higher energies at all L-shells. They identify six enhancement events for 243 keV electron observations at $L = 2.5$. We count five slot region filling events for >292 keV electrons throughout the same year. Turner et al. (2017) finds, however, a somewhat higher occurrence rate (2.5 per month at 200 keV) in the period 2012 to 2016, but confirms the strong energy dependence. The number of observed events decreases exponentially with increasing electron energy for >100 keV. Moreover, we find that there is a significant drop in the occurrence rate in the deep solar minimum from 2007 to 2009 as seen in Table 1 and Figure 8. Here no events are identified for >292 keV fluxes. The same applies to the unusual geomagnetic quiet year of 2014. The respective solar cycle dependence might imply a dependence on the solar wind structures. Figure 9 shows that the slot region filling events are equally distributed between CIR/HSS and CME for >43 keV electrons. However, >292 keV events are more likely to be associated with CMEs.

The superposed epoch analysis of the geomagnetic indices and solar wind parameters in Figure 10 reveals that the slot region filling events are associated with a calm before the storm, negative Bz, and a prominent but gradual solar wind speed increase. This is particularly pronounced for the >292 keV events. A calm period before a storm may be important for preconditioning the magnetosphere for the ensuing mass convection observed during the storm itself. During a quiet geomagnetic period of approximately 2 days or more, ionospheric outflows produce a dense and radially extended plasmasphere, which will lead to higher radiation belt electron precipitation during the initial storm phase due to loss cone scattering by a variety of plasma waves (Borovsky & Steinberg, 2006). As seen in Figure 4 the quiet interval co-exists with a decay of precipitating >43 keV fluxes at all latitudes, however, less prominent at higher energies >114 and >292 keV fluxes. Calm intervals tend to occur when uncompressed slow solar wind precedes the CIRs (Borovsky & Steinberg, 2006). Moreover, the gradual solar wind increase is also characteristic of CIR events, whereas CMEs are often characterized by more abrupt, shock-like features (Kataoka & Miyoshi, 2006). Shock-like features will, however, be averaged out on the daily scale applied in this study. Interestingly, Figure 10 shows that the differences in the geomagnetic indices are small when sorting the events by their solar wind drivers. The stronger solar winds associated with CIRs and the stronger southward component of the CMEs, results in similar geomagnetic disturbances. In particular, Kp is on average nearly identical for the two solar wind drivers for the >43, >114, and >292 keV slot region events. Kp is known to be strongly correlated with magnetospheric convection (Thomsen, 2004). This fuels the discussion on the cause and predictability of slot region filling events. It supports the hypothesis of for example, Zhao and Li (2013) that the flux enhancement in the inner belt and slot region is dependent on inward radial transport.

4.2. Filling and Reforming the Slot Region

Based on Van Allen Probes observations, Reeves et al. (2016) shows that the inner boundary of the outer radiation belt has an S-shaped profile as function of electron energy during quiet times, consistent with >292 keV reaching lower L-values compared to >43 keV as seen in Figure 5 prior to the slot filling event (Day -2). In the slot region filling phase, Days 0–2, however, >43 keV electrons show a strong intensification reaching lower CGM latitudes compared to >292 keV electrons. The rapid intensification might be associated with substorm injections. Turner et al. (2015) attributed the deep injection of electrons in a case study to a two-step process involving dispersionless substorm injections and further transport by fast magnetosonic wave at Pi2 frequencies. A more extensive analysis of the governing mechanism is, however, out of scope of the current analysis, as the data is not sufficient to form a conclusion.

The loss of electron fluxes after a slot region filling event starts immediately (Reeves et al., 2016). This is clearly evident in Figure 5. The most intense precipitation both inside and outside of the predicted plasmapause is found

at the zero and throughout the second epoch day for the >43 and >292 keV BLC fluxes, respectively. This is consistent with the increased intensification of wave-particle interactions of both the chorus whistler mode and plasmaspheric hiss in geomagnetic disturbed periods. For >292 keV the maximum precipitating fluxes is delayed a day or two, owing to the time it takes to accelerate the electrons to the respective energies (Nesse Tyssøy et al., 2021; Salice et al., 2023) suggesting that it is partly a product of accelerated seed particles tens of keV electrons. In the following days, both the precipitation from the main radiation belt and the slot region subside. The relative decrease is more prominent outside the plasmapause compared to inside the plasmasphere, where the latter appears as a near-steady drizzle until the slot region is again devoid of electrons.

A local precipitation minimum at latitudes equatorward of the modelled plasmapause emerges around day four. The local minimum occurs at lower latitudes/deeper into the plasmasphere for higher energies. Reeves et al. (2016) shows that at $L = 4$, the lifetime at 300 keV is shorter than at 40 keV. Moreover, at $L = 3$ the fluxes of 300 keV decrease more quickly than the fluxes of 40 keV, consistent with the slot region recovery seen in Figure 5 on Days >4. These energy- and latitude/L-shell dependent loss rates create the S-shaped outer belt boundary. The two-band structure is evident at all MLTs. However, for the >43 keV fluxes, the wave-particle scattering appears to be less efficient in the morning sector from ~3–9 MLT, resulting in a minimum of EEP fluxes in the slot region. This pattern is opposite of the expected whistler mode chorus wave efficiency, which is clearly evident in the main precipitation region associated with the heart of the radiation belt. The maximum precipitation inside the plasmasphere occurs around noon and in the afternoon/midnight sector. The average wave intensity of plasmaspheric hiss is largest on the dayside in particular during low geomagnetic activity (Meredith et al., 2018) consistent with the recovery period in Figure 5. Moreover, the afternoon/evening intensification in the precipitation is in line with the generation and propagation of lightning-generated whistler mode waves (Záhlava et al., 2019). A potential contribution from electromagnetic ion-cyclotron (EMIC) waves cannot be ruled out based on the MLT pattern. EMIC waves tend to exist inside the plasmasphere with peak wave occurrence in the afternoon sector (~13 < MLT <18) (Meredith et al., 2014; Usanova et al., 2012, 2013). However, as it is generated where an anisotropic ring current coexists with the cold plasmaspheric ions, it is likely to diminish in the recovery phase of the geomagnetic activity. Hence, based on the MLT dependence, the EEP from the slot region is likely to be caused by plasmaspheric hiss and lightning-generated whistler mode waves.

The MLT dependence in Figure 5 is more prominent than observed by the ground-based radar at Rothera in Antarctica by Kavanagh et al. (2018). The ionization level estimated from the medium-frequency (MF) radar is, however, strongly affected by solar illumination. As such, although their analysis was restricted to low solar zenith angles, it might be hard to reveal relatively subtle MLT dependencies found in this study. Nevertheless, Kavanagh et al. (2018) concludes that the EEP from the slot region is likely to be caused by the plasmaspheric hiss in line with our assessment.

In terms of duration, we find that the maximum flux level below 57° CGM latitude ($L < \sim3$), was reduced to 25% of the level found at day zero after 13, 14, and 17 days for the >43, >114, and >292 keV BLC fluxes, respectively. The corresponding e-folding decay rates are ~9, 10, and 12 days. Similar decay rates are estimated from for example, Solar Anomalous and Magnetospheric Particle Explorer observations of electron energies >600 keV and calculation based on a simple drift-diffusion model inside the plasmasphere (Selesnick et al., 2003). Note, however, that the calculated lifetime may be due to a number of different loss mechanisms, for example, pitch angle diffusion, change in energy due to nonlinear effects, inward radial transport etc. Claudepierre et al. (2020) calculated the decay time for electrons over a wide range of energies and L-shells based on Van Allen Probes Observations. They show that the decay rate can be both longer and shorter as function of energy and L-shell. Our estimate is based on electron precipitation from CGM 50–55° corresponding to roughly $L = 2.5$–3. This appears like a transition region where the decay rates change from being consecutive longer to shorter as function of energy. Hence, the consecutive longer decay rates as function energy found in this study should be interpreted with caution.

The apparent energy-dependent decay rates are, however, not evident in Kavanagh et al. (2018). The change in signal-to-noise ratio observed by the MF-radar observation lasts for 11 days before approaching pre-event levels above 72.5 km. Below 66.5 km the change in the signal-to-noise ratio is prominent for only 5 days. It is, however, not certain that the respective slot region filling events will impact the lower altitude levels. As such, it is hard to evaluate if the short period of enhanced ionization at 66.5 km is contradictory to our result of an e-folding decay rate that increases from ~9 to ~12 days for >43 and >292 keV, respectively. Moreover, Figures 4, 5, and 7, show that the reformation of the slot region is dependent on both energy and CGM latitude. The gradually evolving

band, devoid of energetic electrons, is located deeper into the plasmasphere for higher energy electrons. This is consistent with the case study based on Van Allen Probes satellites by Reeves et al. (2016). Hence, the ionization rates confined to a specific geomagnetic latitude will be influenced by the relative distance to the plasmapause.

4.3. The Chemical Imprint of Precipitation From the Slot Region

Despite its frequent nature, EEP from slot region filling events are not included in current EEP parameterizations for chemistry climate models. In the solar forcing recommended for CMIP6 (Matthes et al., 2017), the >30 keV EEP is scaled by Ap (van de Kamp et al., 2016). They apply the plasmapause model by Moldwin et al. (2002) to determine the equatorward extent of the precipitation region. The respective ApEEP forcing was part of the HEPPA III intercomparison project Nesse Tyssøy et al. (2022) which compared eight different EEP estimates based on MEPED during a geomagnetic active period in April 2010. The study revealed that there is large uncertainty in the latitudinal extent of the precipitation region as well as a potential low latitude precipitation band. The CMIP6 parameterization provided the most conservative estimate in both flux intensity and the equatorward extent of the precipitation region. The three EEP estimates based on both the 0° and 90°, however, predicted a much wider precipitation region. Especially, in the main phase of the storm, the deep equatorward precipitation is consistent with a slot region filling event. Afterwards, a noticeable local maximum at low latitudes creating a double oval was found in the EEP estimates based on both the 0° and 90°. In the recovery phase of a storm, the pitch angle scattering rates are expected to be relative weak compared to the main phase. This will result in a strong anisotropic pitch angle distribution within the loss cone, which might explain why the secondary EEP region is not evident in the ionization rates based on the 0° detector. On the other hand, a recent idealized model study by Selesnick et al. (2020) evaluated the angular response functions for POES MEPED electron fluxes. They point out that the sensitivity of the 0° detector outside the nominal field of view may cause the 0° detector to be dominated by quasi-trapped or trapped electrons during periods of weak pitch angle diffusion exaggerating the 0° detector fluxes. The problem is expected to be less prominent at low L-shells due to the change in geometry between the telescopes and the magnetic field. However, to ensure that the estimated EEP from the slot region is not an artefact of the methods applied, Nesse Tyssøy et al. (2022) argues that independent observations are needed to validate the low latitude precipitation.

Kavanagh et al. (2018) identifies 54 cases of slot region filling events, where 20 cases were also detected by an MF radar located at Rothera in Antarctica ($L = 2.7$). Changes in the signal-to-noise ratio, corresponding to increased ionization, persist for around 10 days on average. The impact was detected all the way down to about 55 km. Similarly, we can use the chemical impact of EEP as a mean to validate the precipitation associated with slot region filling events. The quasi-continuous NO 5.3 μm nominal MIPAS observations from 2005 to 2012 provide a global latitude coverage of the lower mesosphere up to 70 km. The observation overlaps with 36 of our identified slot region filling events. Despite the relatively high noise level in the NO data, there is on average a visible NO increase for about 4 days starting at zero epoch. The NO increase occurs before a rise in the solar flare index, which together with typically slow residual transport rates from above, provides strong evidence that the increased NO level at low latitudes corresponds to increased EEP >300 keV.

The challenge is, however, to evaluate the persistence of the increased NO production. The lifetime of the NO molecule is largely determined by photolysis, which implies a lifetime strongly dependent on the season. Hence, during winter the daily NO density is a product of the accumulated EEP over the preceding days. This is clearly evident in Figure 13 where weaker, shorter EEP slot region events during winter, gives a stronger more long-lasting NO change compared to summer. Here, the enhanced NO density persists on average for 10 days in line with increased EEP flux. However, the winter residual circulation will transport NO produced at altitudes above 70 km into the lower mesosphere. Hence, alongside an elevated solar flare index for the winter events, we are unable to conclude if the apparent increase beyond four-five days is truly a consequence of the EEP from the slot region. During summer the increased NO level is only apparent up to 4–5 days, despite a longer persistency of the estimated EEP fluxes. The NO production level is below the MIPAS sensitivity capability.

Moreover, during winter the NO density and its impact on the stratospheric ozone will be strongly affected by the proximity of EEP to the polar vortex. The vortex acts as a horizontal transport barrier containing the EEP-produced NO molecules to mid/polar latitude reducing the potential photolysis. The efficiency of the downward transport to the ozone-rich stratosphere is also linked to the large-scale circulation associated with the vortex. As the polar vortex is oriented geographically and the slot region filling events is oriented geomagnetically, the

different hemispheric offsets between the two coordinate systems might affect the impact of slot regions filling events. As such, the contribution of slot region filling events to the atmospheric chemistry are likely to be most important in the Southern Hemisphere where a larger fraction of the associated EEP will overlap with the vortex (Kavanagh et al., 2018).

A recent study by Zúñiga López et al. (2022) based on the Whole Atmosphere Community Climate Model, demonstrates that EEP ionization rates (>30 keV) impact mesospheric OH and ozone mixing ratios, which leads to changes in mesospheric temperature, zonal wind and the residual circulation. The required fluxes of EEP to impose dynamical changes depend on the dynamical preconditions. During the Northern Hemispheric winter, even weak ionization rates can modulate the mesospheric signal of a sudden stratospheric warming event. Further analysis is required to determine the impact of slot region filling events on atmospheric chemistry. Hence, to fully evaluate the potential impact of the relatively weak fluxes of EEP from the slot region, further analysis is required.

5. Conclusion

BLC estimates based on both 0° and 90° telescopes of MEPED onboard NOAA/POES, allow us to study the EEP associated with slot region filling events. We identify 65, 56, and 32 >43, >114, and >292 keV events, respectively. In line with previous studies, the occurrence rate is strongly energy dependent. Moreover, the occurrence rate drops during solar minimum, where it is zero for the >292 keV events. The solar wind drivers can be both CME and/or CIR/HSS. The >292 keV events are likely to be associated with CME.

Superposed epoch analysis reveals that the >292 keV events are associated with stronger geomagnetic deflections. Moreover, solar wind speed, IMF Bz, and Ey reveal a period of calm before the storm, which is potentially important for preconditioning the magnetosphere for the ensuing mass convection observed during the storm itself. Independent of the solar wind drivers, the geomagnetic indices are similar. This similarity is particularly evident in the Kp index, which is known to be strongly correlated with magnetospheric convection. However, no single mechanism can account for filling and recovery of the EEP slot region observations. It is likely that several different mechanisms are acting together both in the slot region filling phase as well as the slot region recovery phase.

The slot region reforms more efficiently closer to the plasmapause, which creates a double EEP band throughout the recovery period. The maximum flux level below 57° CGM latitude ($L < 3$), was reduced to 25% of the level found at day zero after 13, 14 and 17 days for the >43, >114, and >292 keV BLC fluxes, respectively. The corresponding e-folding decay rates are approximately 9, 10, and 12 days consistent with previous studies. The slot region precipitation pattern maximizes around noon throughout the afternoon/evening sector, consistent with pitch angle scattering into the loss cone from plasmaspheric hiss and lightning-induced whistler mode waves.

It is evident that the NO density increases during both summer and winter at low latitudes associated with slot region filling events. The NO levels stay elevated for at least 4 days independent of season. The NO density will, however, depend on both the flux of EEP in the slot region as well as the level of photolysis. Potential NO transport from above and additional ionization associated with solar flares make it challenging to evaluate to which degree the weak drizzle of electrons in the geomagnetic quiet period after the main storm period contributes to the NO density. More research on potential atmospheric impact is required.

Data Availability Statement

References

Babu, E. M., Tyssøy, H. N., Smith-Johnsen, C., Maliniemi, V., Salice, J. A., Millan, R. M., & Richardson, I. G. (2022a). Determining latitudinal extent of energetic electron precipitation using MEPED on-board NOAA/POES. *Journal of Geophysical Research: Space Physics*, *127*(9), e2022JA030489. https://doi.org/10.1029/2022JA030489

Babu, E. M., Tyssøy, H. N., Smith-Johnsen, C., Maliniemi, V., Salice, J. A., Millan, R. M., & Richardson, I. G. (2022b). Determining latitudinal extent of energetic electron precipitation using MEPED on-board NOAA/POES [Dataset]. Zenodo. https://doi.org/10.5281/zenodo.6590387

Baker, D., Kanekal, S., Li, X. E. A., Monk, S. P., Goldstein, J., & Burch, J. L. (2004). An extreme distortion of the Van Allen belt arising from the "halloween" solar storm in 2003. *Nature*, *432*(7019), 878–881. https://doi.org/10.1038/nature03116

Borovsky, J. E., & Steinberg, J. T. (2006). The "calm before the storm" in CIR/magnetosphere interactions: Occurrence statistics, solar wind statistics, and magnetospheric preconditioning. *Journal of Geophysical Research*, *111*(A7), A07S10. https://doi.org/10.1029/2005JA011397

Brasseur, G., & Solomon, S. (2005). *Aeronomy of the middle atmosphere–chemistry and physics of the stratosphere and mesosphere, atmospheric and oceanographic sciences library 32* (Vol. 17, p. 3300). Springer.

Carson, B. R., Rodger, C. J., & Clilverd, M. A. (2013). Poes satellite observations of emic-wave driven relativistic electron precipitation during 1998–2010. *Journal of Geophysical Research: Space Physics*, *118*(1), 232–243. https://doi.org/10.1029/2012JA017998

Chen, Z., Tian, H., Li, H., Tang, R., Ouyang, Z., & Deng, X. (2023). The study on the global evolution of energetic electron precipitation during geomagnetic storm based on deep learning algorithm. *Journal of Geophysical Research: Space Physics*, *128*(3), e2022JA030974. https://doi.org/10.1029/2022JA030974

Claudepierre, S. G., Ma, Q., Bortnik, J., O'Brien, T. P., Fennell, J. F., & Blake, J. B. (2020). Empirically estimated electron lifetimes in the Earth's radiation belts: Van Allen probe observations. *Geophysical Research Letters*, *47*(3), e2019GL086053. https://doi.org/10.1029/2019GL086053

Evans, D. S., & Greer, M. S. (2004). *Polar orbiting environmental satellite space environment monitor—2: Instrument descriptions and archive data documentation version 1.4* (p. 93). NOAA Technical Memorandum.

Fischer, H., Birk, M., Blom, C., Carli, B., Carlotti, M., von Clarmann, T., et al. (2008). MIPAS: An instrument for atmospheric and climate research. *Atmospheric Chemistry and Physics*, *8*(8), 2151–2188. https://doi.org/10.5194/acp-8-2151-2008

Funke, B., García-Comas, M., Glatthor, N., Grabowski, U., Kellmann, S., Kiefer, M., et al. (2022). MIPAS IMK/IAA version 8 retrieval of nitric oxide and lower thermospheric temperature. *Atmospheric Measurement Techniques*, https://doi.org/10.5194/amt-2022-260

Kataoka, R., & Miyoshi, Y. (2006). Flux enhancement of radiation belt electrons during geomagnetic storms driven by coronal mass ejections and corotating interaction regions. *Space Weather*, *4*(9), 09004. https://doi.org/10.1029/2005SW000211

Kavanagh, A. J., Cobbett, N., & Kirsch, P. (2018). Radiation belt slot region filling events: Sustained energetic precipitation into the mesosphere. *Journal of Geophysical Research: Space Physics*, *123*(9), 7999–8020. https://doi.org/10.1029/2018JA025890

Kennel, C. F., & Petschek, H. E. (1966). Limit on stably trapped particle fluxes. *Journal of Geophysical Research*, *71*(1), 1–28. https://doi.org/10.1029/JZ071i001p00001

Kim, K.-C., Shprits, Y., Subbotin, D., & Ni, B. (2011). Understanding the dynamic evolution of the relativistic electron slot region including radial and pitch angle diffusion. *Journal of Geophysical Research*, *116*(A10), A10214. https://doi.org/10.1029/2011JA016684

Lam, M. M., Horne, R. B., Meredith, N. P., Glauert, S. A., Moffat-Griffin, T., & Green, J. C. (2010). Origin of energetic electron precipitation >30 kev into the atmosphere. *Journal of Geophysical Research*, *115*(A4), A00F08. https://doi.org/10.1029/2009JA014619

Li, H., Yuan, Z., Wang, D., Huang, S., Qiao, Z., & Yu, X. (2016). Statistical characteristics of potentially chorus-driven energetic electron precipitation from POES observations. *Journal of Geophysical Research: Space Physics*, *121*(10), 9531–9546. https://doi.org/10.1002/2016JA023101

Liu, X., Liu, W., Cao, J. B., Fu, H. S., Yu, J., & Li, X. (2015). Dynamic plasmapause model based on THEMIS measurements. *Journal of Geophysical Research: Space Physics*, *120*(12), 10543–10556. https://doi.org/10.1002/2015JA021801

Lyons, L. R., & Thorne, R. M. (1973). Equilibrium structure of radiation belt electrons. *Journal of Geophysical Research*, *78*(13), 2142–2149. https://doi.org/10.1029/JA078i013p02142

Maliniemi, V., Asikainen, T., & Mursula, K. (2016). Effect of geomagnetic activity on the northern annular mode: Qbo dependence and the Holton-tan relationship. *Journal of Geophysical Research: Atmospheres*, *121*(17), 10043–10055. https://doi.org/10.1002/2015JD024460

Matthes, K., Funke, B., Anderson, M., Barnard, L., Beer, J., Charbonneau, P., et al. (2017). Solar forcing for CMIP-6. *Geoscientific Model Development*, *10*(6), 2247–2302. https://doi.org/10.5194/gmd-10-2247-2017

Meredith, N. P., Horne, R. B., Glauert, S. A., Baker, D. N., Kanekal, S. G., & Albert, J. M. (2009). Relativistic electron loss timescales in the slot region. *Journal of Geophysical Research*, *114*(A3), A03222. https://doi.org/10.1029/2008JA013889

Meredith, N. P., Horne, R. B., Kersten, T., Fraser, B. J., & Grew, R. S. (2014). Global morphology and spectral properties of emic waves derived from CRRES observations. *Journal of Geophysical Research: Space Physics*, *119*(7), 5328–5342. https://doi.org/10.1002/2014JA020064

Meredith, N. P., Horne, R. B., Kersten, T., Li, W., Bortnik, J., Sicard, A., & Yearby, K. H. (2018). Global model of plasmaspheric hiss from multiple satellite observations. *Journal of Geophysical Research: Space Physics*, *123*(6), 4526–4541. https://doi.org/10.1029/2018JA025226

Moldwin, M. B., Downward, L., Rassoul, H., Amin, R., & Anderson, R. (2002). A new model of the location of the plasmapause: CRRES results. *Journal of Geophysical Research*, *107*(A11), 1339. https://doi.org/10.1029/2001JA009211

Nesse Tyssøy, H., Partamies, N., Babu, E. M., Smith-Johnsen, C., & Salice, J. A. (2021). The predictive capabilities of the auroral electrojet index for medium energy electron precipitation. *Frontiers in Astronomy and Space Sciences*, *8*. https://doi.org/10.3389/fspas.2021.714146

Nesse Tyssøy, H., Sandanger, M. I., Ødegaard, L.-K. G., Stadsnes, J., Aasnes, A., & Zawedde, A. E. (2016). Energetic electron precipitation into the middle atmosphere—Constructing the loss cone fluxes from MEPED POES. *Journal of Geophysical Research: Space Physics*, *121*(6), 5693–5707. https://doi.org/10.1002/2016JA022752

Nesse Tyssøy, H., Sinnhuber, M., Asikainen, T., Bender, S., Clilverd, M. A., Funke, B., et al. (2022). Heppa iii intercomparison experiment on electron precipitation impacts: 1. Estimated ionization rates during a geomagnetic active period in April 2010. *Journal of Geophysical Research: Space Physics*, *127*(1), e2021JA029128. https://doi.org/10.1029/2021JA029128

Ødegaard, L.-K. G., Tyssøy, H. N., Sandanger, M. I. J., Stadsnes, J., & Søraas, F. (2016). Space weather impact on the degradation of NOAA POES MEPED proton detectors. *Journal of Space Weather and Space Climate*, *6*, A26. https://doi.org/10.1051/swsc/2016020

Ødegaard, L.-K. G., Tyssøy, H. N., Søraas, F., Stadsnes, J., & Sandanger, M. I. (2017). Energetic electron precipitation in weak to moderate corotating interaction region-driven storms. *Journal of Geophysical Research: Space Physics*, *122*(3), 2900–2921. https://doi.org/10.1002/2016JA023096

Reeves, G. D., Friedel, R. H. W., Larsen, B. A., Skoug, R. M., Funsten, H. O., Claudepierre, S. G., et al. (2016). Energy-dependent dynamics of KeV to MeV electrons in the inner zone, outer zone, and slot regions. *Journal of Geophysical Research: Space Physics*, *121*(1), 397–412. https://doi.org/10.1002/2015JA021569

Richardson, I. G., & Cane, H. V. (2012). Near-Earth solar wind flows and related geomagnetic activity during more than four solar cycles (1963-2011). *Journal of Space Weather and Space Climate*, *2*, A02. https://doi.org/10.1051/swsc/2012003

Ripoll, J.-F., Chen, Y., Fennell, J. F., & Friedel, R. H. W. (2015). On long decays of electrons in the vicinity of the slot region observed by HEO3. *Journal of Geophysical Research: Space Physics*, *120*(1), 460–478. https://doi.org/10.1002/2014JA020449

Rodger, C., Clilverd, M., Green, J., & Lam, M. (2010). Use of POES SEM-2 observations to examine radiation belt dynamics and energetic electron precipitation into the atmosphere. *Journal of Geophysical Research*, *115*(A4), A04202. https://doi.org/10.1029/2008JA014023

Rozanov, E., Calisto, M., Egorova, T., Peter, T., & Schmutz, W. (2012). Influence of the precipitating energetic particles on atmospheric chemistry and climate. *Surveys in Geophysics*, *33*(3–4), 483–501. https://doi.org/10.1007/s10712-012-9192-0

Salice, J., Nesse, H., Babu, E., Smith-Johnsen, C., & Richardson, I. (2023). Exploring the predictability of the high-energy tail of MEE precipitation based on solar wind properties. *Journal of Geophysical Research: Space Physics*, *128*(3), e2022JA031194. https://doi.org/10.1029/2022JA031194

Sandanger, M. I., Ødegaard, L.-K. G., Nesse Tyssøy, H., Stadsnes, J., Søraas, F., Oksavik, K., & Aarsnes, K. (2015). In-flight calibration of NOAA POES proton detectors—Derivation of the MEPED correction factors. *Journal of Geophysical Research: Space Physics*, *120*(11), 9578–9593. https://doi.org/10.1002/2015JA021388

Sætre, C., Stadsnes, J., Nesse, H., Aksnes, A., Petrinec, S. M., Barth, C. A., & Østgaard, N. (2004). Energetic electron precipitation and the no abundance in the upper atmosphere: A direct comparison during a geomagnetic storm. *Journal of Geophysical Research*, *109*(A9), A09302. https://doi.org/10.1029/2004JA010485

Selesnick, R. S., Blake, J. B., & Mewaldt, R. A. (2003). Atmospheric losses of radiation belt electrons. *Journal of Geophysical Research*, *108*(A12), 1468. https://doi.org/10.1029/2003JA010160

Selesnick, R. S., Tu, W., Yando, K., Millan, R. M., & Redmon, R. J. (2020). POES/MEPED angular response functions and the precipitating radiation belt electron flux. *Journal of Geophysical Research: Space Physics*, *125*(9), e2020JA028240. https://doi.org/10.1029/2020JA028240

Seppälä, A., Lu, H., Clilverd, M. A., & Rodger, C. J. (2013). Geomagnetic activity signatures in wintertime stratosphere wind, temperature, and wave response. *Journal of Geophysical Research: Atmospheres*, *118*(5), 2169–2183. https://doi.org/10.1002/jgrd.50236

Seppälä, A., Randall, C. E., Clilverd, M. A., Rozanov, E., & Rodger, C. J. (2009). Geomagnetic activity and polar surface air temperature variability. *Journal of Geophysical Research*, *114*(A10), A10312. https://doi.org/10.1029/2008JA014029

Sinnhuber, M., Nieder, H., & Wieters, N. (2012). Energetic particle precipitation and the chemistry of the mesosphere/lower thermosphere. *Surveys in Geophysics*, *33*(6), 1281–1334. https://doi.org/10.1007/s10712-012-9201-3

Smith-Johnsen, C., Nesse Tyssøy, H., Hendrickx, K., Orsolini, Y., Kumar, G., Glesnes Ødegard, L.-K., et al. (2017). Direct and indirect electron precipitation effect on nitric oxide in the polar middle atmosphere using a full-range energy spectrum. *Journal of Geophysical Research: Space Physics*, *122*(8), 8679–8693. https://doi.org/10.1002/2017JA024364

Theodoridis, G., & Paolini, F. (1967). Pitch angle diffusion of relativistic outer belt electrons. *Annales de Geophysique*, *23*.

Thomsen, M. F. (2004). Why Kp is such a good measure of magnetospheric convection. *Space Weather*, *2*(11), S11004. https://doi.org/10.1029/2004SW000089

Thorne, R. M., Shprits, Y. Y., Meredith, N. P., Horne, R. B., Li, W., & Lyons, L. R. (2007). Refilling of the slot region between the inner and outer electron radiation belts during geomagnetic storms. *Journal of Geophysical Research*, *112*(A6), A06203. https://doi.org/10.1029/2006JA012176

Turner, D. L., Claudepierre, S. G., Fennell, J. F., O'Brien, T. P., Blake, J. B., Lemon, C., et al. (2015). Energetic electron injections deep into the inner magnetosphere associated with substorm activity. *Geophysical Research Letters*, *42*(7), 2079–2087. https://doi.org/10.1002/2015GL063225

Turner, D. L., O'Brien, T. P., Fennell, J. F., Claudepierre, S. G., Blake, J. B., Jaynes, A. N., et al. (2017). Investigating the source of near-relativistic and relativistic electrons in Earth's inner radiation belt. *Journal of Geophysical Research: Space Physics*, *122*(1), 695–710. https://doi.org/10.1002/2016JA023600

Usanova, M. E., Darrouzet, F., Mann, I. R., & Bortnik, J. (2013). Statistical analysis of emic waves in plasmaspheric plumes from cluster observations. *Journal of Geophysical Research: Space Physics*, *118*(8), 4946–4951. https://doi.org/10.1002/jgra.50464

Usanova, M. E., Mann, I. R., Bortnik, J., Shao, L., & Angelopoulos, V. (2012). Themis observations of electromagnetic ion cyclotron wave occurrence: Dependence on AE, SYMH, and solar wind dynamic pressure. *Journal of Geophysical Research*, *117*(A10), A10218. https://doi.org/10.1029/2012JA018049

van de Kamp, M., Rodger, C. J., Seppälä, A., Clilverd, M. A., & Verronen, P. T. (2018). An updated model providing long-term data sets of energetic electron precipitation, including zonal dependence. *Journal of Geophysical Research: Atmospheres*, *123*(17), 9891–9915. https://doi.org/10.1029/2017JD028253

van de Kamp, M., Seppälä, A., Clilverd, M. A., Rodger, C. J., Verronen, P. T., & Whittaker, I. C. (2016). A model providing long-term data sets of energetic electron precipitation during geomagnetic storms. *Journal of Geophysical Research: Atmospheres*, *121*(20), 12520–12540. https://doi.org/10.1002/2015JD024212

Walton, S. D., Forsyth, C., Rae, I. J., Watt, C. E. J., Thompson, R. L., Horne, R. B., et al. (2021). Cross-coherence of the outer radiation belt during storms and the role of the plasmapause. *Journal of Geophysical Research: Space Physics*, *126*(10), e2021JA029308. https://doi.org/10.1029/2021JA029308

Whittaker, I. C., Clilverd, M. A., & Rodger, C. J. (2014). Characteristics of precipitating energetic electron fluxes relative to the plasmapause during geomagnetic storms. *Journal of Geophysical Research: Space Physics*, *119*(11), 8784–8800. https://doi.org/10.1002/2014JA020446

Whittaker, I. C., Rodger, C. J., Clilverd, M. A., & Sauvaud, J.-A. (2014). The effects and correction of the geometric factor for the POES/MEPED electron flux instrument using a multisatellite comparison. *Journal of Geophysical Research: Space Physics*, *119*(8), 6386–6404. https://doi.org/10.1002/2014JA020021

Xu, W., Marshall, R. A., Tyssøy, H. N., & Fang, X. (2020). A generalized method for calculating atmospheric ionization by energetic electron precipitation. *Journal of Geophysical Research: Space Physics*, *125*(11), e2020JA028482. https://doi.org/10.1029/2020JA028482

Yando, K., Millan, R. M., Green, J. C., & Evans, D. S. (2011). A Monte Carlo simulation of the NOAA POES medium energy proton and electron detector instrument. *Journal of Geophysical Research*, *116*(A10), A10231. https://doi.org/10.1029/2011JA016671

Záhlava, J., Němec, F., Santolík, O., Kolmašová, I., Hospodarsky, G. B., Parrot, M., et al. (2019). Lightning contribution to overall whistler mode wave intensities in the plasmasphere. *Geophysical Research Letters*, *46*(15), 8607–8616. https://doi.org/10.1029/2019GL083918

Zawedde, A. E., Nesse Tyssøy, H., Hibbins, R., Espy, P. J., Ødegaard, L.-K. G., Sandanger, M. I., & Stadsnes, J. (2016). The impact of energetic electron precipitation on mesospheric hydroxyl during a year of solar minimum. *Journal of Geophysical Research: Space Physics*, *121*(6), 5914–5929. https://doi.org/10.1002/2016JA022371

Zawedde, A. E., Nesse Tyssøy, H., Stadsnes, J., & Sandanger, M. I. (2019). Are EEP events important for the tertiary ozone maximum? *Journal of Geophysical Research: Space Physics*, *124*(7), 5976–5994. https://doi.org/10.1029/2018JA026201

Zhao, H., & Li, X. (2013). Modeling energetic electron penetration into the slot region and inner radiation belt. *Journal of Geophysical Research: Space Physics*, *118*(11), 6936–6945. https://doi.org/10.1002/2013JA019240

Zúñiga López, H. D., Tyssøy, H. N., Smith-Johnsen, C., & Maliniemi, V. (2022). The direct effect of medium energy electron precipitation on mesospheric dynamics during a sudden stratospheric warming event in 2010. *Geophysical Research Letters*, *49*(13), e2022GL097812. https://doi.org/10.1029/2022GL097812